Multiscale characterization of *Caenorhabditis elegans* mutants to probe functional mechanisms of human actin pathological variants

Théo Hecquet[1,2,3,4], Nadine Arbogast[1,2,3,4], Delphine Suhner[1,2,3,4], Anaïs Goetz[1,2,3,4], Grégory Amann[1,2,3,4], Selin Yürekli[1,2,3,4], Fiona Marangoni[1,2,3,4], Sophie Quintin[1,2,3,4], Johannes N. Greve[5], Nataliya Di Donato[6], Anne-Cécile Reymann[1,2,3,4,7]*

1. Université de Strasbourg, IGBMC UMR 7104- UMR-S 1258, F-67400 Illkirch, France
2. CNRS, UMR 7104, F-67400 Illkirch, France
3. Inserm, UMR-S 1258, F-67400 Illkirch, France
4. IGBMC, Institut de Génétique et de Biologie Moléculaire et Cellulaire, F-67400 Illkirch, France
5. Institute for Biophysical Chemistry, Hannover Medical School, Fritz–Hartmann–Centre for Medical Research, 30625 Hannover, Germany
6. Department of Human Genetics, Hannover Medical School, 30§625 Hannover, Germany
7. Lead contact

*Correspondence: reymanna@igbmc.fr

SUMMARY

Actin plays a crucial role in diverse physiological processes by forming dynamic networks that determine cellular shape and mechanical properties. Non-Muscle Actinopathies (NMA) are rare diseases caused by *de novo* variants in human cytoskeletal β-actin (*ACTB*) and γ-actin (*ACTG1*) genes, ranging from missense mutations to whole gene deletions. Currently, the high clinical variability and genotype-phenotype correlations in NMA remain largely unresolved. To address this concern, we inserted nine mutations identified in patients in the *C. elegans* cytoplasmic actin orthologue *act-2* and performed a quantitative multiscale characterization of these animal models. We uncovered various perturbations including micro-scale actin network defects, cell-scale abnormalities, morphogenesis failure, and weaker behavioural phenotypes. Notably, the severity of the observed defects correlates with the severity of patients' symptoms. Thus, we provide evidence that such *C. elegans* models are relevant to investigate the mechanisms underlying NMA physiopathology and could ultimately be used to screen for therapeutic strategies.

KEYWORDS

C. elegans, cytoplasmic actin, rare disease, Non-Muscle Actinopathy, Baraitser-Winter Cerebrofrontofacial Syndrome

INTRODUCTION

The ability to dynamically assemble the actin cytoskeleton in response to internal and external triggers is a hallmark of a healthy and functional cell. Finely tuned actin architectures are coordinated to fulfil specific cellular needs and drive a multitude of cellular processes including motility, adhesion, morphogenesis, mechanotransduction, internal organisation and trafficking[1–4]. Constant reorganization for adapting to external cues is intrinsically linked to the capacity of cytoskeletal actin networks to turnover and to reorganise, typically in the scale of seconds or minutes[3]. Altered cytoskeletal integrity or dynamics are implicated in many disorders ranging from hearing loss to cancer or to rare developmental diseases[5,6]. The human genome encodes six highly conserved actin isoforms, which are produced in a time- and tissue-specific manner and every actin isoform has been associated with human pathologies[5]. *De novo* missense variants, frameshift or truncating variants as well as gene deletions in the *ACTB* and *ACTG1* genes, which encode the ubiquitously expressed cytoplasmic β- and γ-actin, cause substantial cellular dysfunction and lead to a range of rare autosomal dominant disorders, termed Non-Muscle Actinopathies (NMA)[7–12]. One particularity of this category of diseases is the broad spectrum of symptoms found in patients. NMA can range from very mild to severe neurological impairment and cortical malformations as well as reduced life expectancy of the affected patients. So far, 290 patients and 157 unique mutations have been reported to cause NMA[13]. The most frequently associated NMA disease, named Baraitser-Winter cerebrofrontofacial syndrome (BWCFF), is associated with characteristic facial malformations, intellectual disability, cortical malformations, epilepsy, hearing loss and a variety of congenital anomalies[10,11]. Even within the BWCFF subclass of NMA, a large range of symptom severity is observed.

To date, a definitive genotype-phenotype correlation within the NMA field has yet to emerge, and the functional mechanisms causing symptoms in patients remain largely elusive. It is likely that the complexity originates from both the multifaceted roles of actin and its numerous molecular partners (Actin Binding Proteins; ABP). Furthermore, the existence of compensatory mechanisms between isoforms constitute a challenge in the study of actin *in vivo*[14–19]. Actin variants have been proposed to affect the cytoskeleton by four mechanisms: insufficient availability of actin monomers, alteration of the actin filament assembly or disassembly kinetics, alteration of actin interactions with binding partners and assembly of toxic actin oligomers detrimental for proper cytoskeletal function[13,20]. The use of purified recombinant human actin proteins allows us to quantitatively assess defects in terms of folding, thermal stability, nucleotide-binding, G- to F-actin transition and interaction with ABPs for some variants[13,20–22], validating some of these hypotheses. At the structural level, *in silico* models correlate some NMA mutations with nucleotide-binding,

68 monomer-monomer interaction and canonical G-actin-ABP interaction surfaces[8]. *In vivo*, the
69 effects of *Actb* and *Actg1* deletions have been studied in mouse embryonic fibroblasts and in the
70 whole animal[23–25]**.** Notably, *Actb* deletion leads to proliferation defects in mouse embryonic
71 fibroblasts as well as embryonic lethality in mice, whereas *Actg1* null mutant mice are viable[26].
72 Currently, however, a comprehensive system capable of bridging these different scales and
73 validating the suggested molecular to functional relationship is still missing.

74 To fill this gap, we chose to use the free-living nematode *Caenorhabditis elegans* (*C. elegans*)
75 as a model to study NMA, as it provides easy access to all biologically relevant scales: from
76 general animal fitness to stereotypical organization and development, up to cell-scale events and
77 single molecular dynamics *in vivo*. *C. elegans* has already been used as a model for numerous
78 diseases, notably for the study of neurodegenerative and neuromuscular disorders[27], validating
79 its relevance for assessing the molecular-to-functional link in pathologies. The ease of genetic
80 manipulation and the ability to obtain stable, isogenic strains within a matter of weeks streamlines
81 the process of strain characterization and enables us to investigate the consequences of multiple
82 NMA variants in a reasonable amount of time.

83 As in humans, *C. elegans* relies on different cytoplasmic actin paralogs to sustain cellular
84 cytoskeleton integrity in all cell types. Three ubiquitously expressed actin genes (*act-1, act-2* and
85 *act-3*) are present in a cluster and operate in a partially redundant manner, notably during early
86 embryogenesis[28–30]. These three cytoplasmic *C. elegans* actins are also required for proper
87 muscle function[31]. Indeed, mutants which carry some *act-2* mutations, exhibit uncoordinated adult
88 movement or pharyngeal pumping defects[29,32–34]. A fourth actin-coding gene named *act-4* is
89 expressed in different tissues, notably in neurons and in muscle cells. However, *act-4* is not as
90 abundant or ubiquitously expressed in the early embryo as expected for an essential cytoplasmic
91 actin such as *act-1 -2, and -3*[18]. By contrast, *act-5* shows a strong tissue-specific expression in
92 the gut and excretory cell[35]. Among the *C. elegans* proteins, ACT-2 has the highest similarity to
93 human cytoplasmic actin proteins, sharing 98% of amino acids with β-actin and 97% with γ-actin.

94 In this study, we assess the consequences of actin variants associated with BWCFF or
95 other NMA in a model organism and present a quantitative multiscale characterization of *C.*
96 *elegans* mutants. As cytoplasmic actin is required pleiotropically, we performed a global survey
97 of mutants using well-established methods to assay both nematode fitness and specific organ
98 function. We propose a classification of selected NMA variants with respect to the observed
99 phenotypes in *C. elegans* and compare this classification to the severity of human patient's
100 symptoms. This initial study of actin variants showed a strong correlation in the degree of

101 pathological severities between *C. elegans* and humans, thus validating the use of *C. elegans* as
102 a tool to study NMA. Importantly, this work paves the way towards the prediction of clinical severity
103 in patients carrying novel actin variants from the outset of diagnosis.

104

105

106 ## RESULTS

107 ### *Generation of C. elegans models recapitulating human non-muscle actinopathies*

108 With respects to the three *C. elegans* cytoplasmic actin genes: while *act-1* and *act-3* share
109 identical coding sequences, they differ from *act-2* by three non-synonymous and many silent
110 variations as well as distinct intronic regions. This allows a slightly easier CRISPR/Cas9 genome
111 editing for *act-2* than for the others[36]. In addition, similarly to its human cytoplasmic actin
112 counterparts (*ACTB* and *ACTG1*), *C. elegans* ACT-2 is most likely present in abundant levels in
113 all cell types. Fluorescence corresponding to the expression of a *GFP::act-2* transgene driven by
114 an *act-2* promoter region is observed in all cells in the early embryo (20 cell stage), in the
115 epidermis as well as in muscle cells[29]. Therefore, we decided to insert a series of genetic
116 modifications identified in the human *ACTB* and *ACTG1* genes in *C. elegans act-2*. In order to
117 span the range of severities observed in human, we chose to study an initial set of eight mutations
118 which included mutations associated with BWCFF (*ACTB* p.L65V, *ACTB* p.G74S, *ACTB* p.G74V,
119 *ACTB* or *ACTG1* p.T120I, *ACTB* p.R196C, *ACTB* p.R196H and *ACTG1* p.T203M)[11,37,38]; as well
120 as non-BWCFF NMA diseases (*ACTB* p.R147S and *ACTB* or *ACTG1* p.R183W) (Figure 1).
121 Among them, *ACTB* p.R196 is a hot-spot identified in over 19 patients, presenting clinical
122 variability with a high degree of brain malformation (83%, Figure 1A)[11,39]. *ACTB* p.R147S
123 represents a hotspot postzygotic disruption causing the mosaic skin disorders known as Becker
124 nevus syndrome[40]. This variant is likely lethal in a homozygous context[41]. *ACTB* p.R183W is
125 associated with dystonia deafness[42–48].

126 We mapped these mutated residues on a structural model of the *C. elegans* ACT-2 monomer
127 (G-actin) and filament to assess the localisation of the variants in different regions of the molecule
128 that correlate with specific functions (Figure 1B). The variants are distributed across all four
129 subdomains (SD) of the actin monomer. Two examined residues (G74, R183) are located within
130 the nucleotide-binding cleft and, although not directly involved in nucleotide coordination or
131 hydrolysis, contribute significantly to the release of inorganic phosphate following ATP
132 hydrolysis[49,50]. The R147 residue is part of the target-binding cleft of the actin monomer, located
133 between SD1 and SD3, which is lined with predominantly hydrophobic residues and represents

134 a main interaction interface for G-actin binding proteins[24,51]. Residue T120 is part of the so-called
135 pathogenic helix of actin (K113-T126), which constitutes a hotspot for mutations in several human
136 actin isoforms leading to BWCFF (cytoskeletal β- and γ-actin), non-syndromic hearing loss
137 (cytoskeletal γ-actin), thoracic aortic aneurysm (smooth muscle α-actin) and nemaline myopathy
138 (skeletal muscle α-actin) (as reviewed in Rubenstein and Wen[52]). Residues R196 and T203 are
139 both located in SD4 and are part of regions of the actin monomer that are heavily involved in the
140 formation of monomer-monomer contacts within the actin filament. The neighbouring residue of
141 R196, E195, forms a salt-bridge with K113 of the laterally opposing monomer. T203 is part of a
142 threonine-rich loop that contributes to lateral and longitudinal contacts in the filament[51,53].
143 Polymerization deficiencies of the p.R196H and p.T203M variant were verified in *in vitro*
144 experiments. These three variants are predicted to impair actin capacity to polymerise into
145 filaments *in vivo* as confirmed by *in vitro* experiments for the ACTB p.R196H T120I and T203M
146 variants[13,22]. The L65 residue is located in SD2 in close proximity to the DNase-loop that
147 contributes to lateral and longitudinal interfaces and undergoes structural rearrangement upon
148 nucleotide hydrolysis, directly affecting filament stability[49,53].

149 Using these selected variants associated with various human symptoms, we generated
150 strains harbouring each NMA mutation in the *act-2* gene, using CRISPR/Cas9 gene editing
151 (Figure 1C, S1A). We verified that no additional mutations were present in the other four actin
152 genes and outcrossed the strains at least four times before analysis. Additionally, we generated
153 two new prospective null alleles for *act-2* (*rey016* and *rey021*) (Figure 1C), each resulting in a
154 premature STOP codon within exon 2 (see methods section for more details). For comparison,
155 we assayed a previously characterized *act-2* knock-out (KO) strain (allele *ok1229*) obtained via
156 an EMS screen, which harbours a larger deletion extending beyond the 3' UTR[29].

157

158 ***ACT-2 missense variants affect the general viability of C. elegans to different degrees***

159 We first compared the general viability of the different mutant *act-2* strains obtained at 20°C.
160 We found that some mutant animals for p.R147S or p.T203M developed into homozygous adults
161 but these few escapers produced very few embryos that were 100% lethal during embryogenesis,
162 suggesting a fully penetrant maternal-effect lethal phenotype. We thus maintained these variants
163 as heterozygous animals using the *nT1* balancer[54]. Interestingly, one mutation (p.G74V) caused
164 lethality in heterozygous state, suggesting a dominant effect for this allele. Indeed, for this variant
165 we obtained very few edited surviving F1 animals after CRISPR injections. Sequencing of several
166 of these F1 edited animals confirmed the presence of a heterozygous G74V variant in the *act-2*

167 gene (Figure S1B); but if some produce very few eggs, none developed into living embryos.
168 Because we were unable to maintain a stable line expressing this variant, we did not pursue its
169 characterization. Surprisingly, another variant affecting the same residue (p.G74S) could be
170 maintained as homozygous. All other variants (p.L65V, p.T120I, p.R183W, p.R196C, p.R196H)
171 as well as the KO *rey016, rey021* and *ok1229* were viable at a homozygous state and were thus
172 maintained as such, although some of them had very few progenies. In conclusion, out of the nine
173 single-point missense variants generated, six could be maintained as homozygous, two as
174 heterozygous and one was inadequately viable (Figure 1D). This initial finding emphasizes how
175 important these variants are in development and health and highlights the remarkable
176 conservation of actin across species.

177

178 ***act-2 gene knock-out affects reproduction and embryo viability***

179 To assess how individual point variants compare with gene KO, we performed a detailed
180 analysis of phenotypes in the absence of ACT-2 protein expression. We assessed both the newly
181 CRISPR generated *act-2* KO strains (*rey016 and rey021* allele) as well as the EMS generated
182 strain, *ok1229*[29]. We first verified in homozygous L4 animals if transcriptional adaptation of
183 another actin coding gene could compensate for the loss of *act-2*, as proposed by Willis and
184 colleagues[29]. Such transcriptional adaptation has been reported in an *act-5* variant[18,19]. Therefore,
185 we measured the expression of mRNA of all actin coding genes using single animal RT-qPCR in
186 L4 animals devoid of embryos, to avoid developmental differences in the experimental read-out[55].
187 We found that both *ok1229* and *rey021* strains show a clear absence of *act-2* mRNA and that for
188 *rey021 act-1* expression was increased compared to wild-type (N2) animals (*rey021 act-1* fold
189 change = 2.6; log2fold change = 1.4), unlike other actins which only had milder fluctuations of
190 expression (Figure 2A). We additionally tested whether compensation could be detected in
191 several *act-2* single-point missense variants. We observed some variable mRNA levels of other
192 actin genes than *act-2* only in presence of the variants p.R147S and p.T203M (homozygous L4
193 assessed), but not for the other variants tested (p.L65V, p.R196C, p.R196H) (Figure 2A). We
194 conclude that there is possibly transcriptional adaptation for actin in *C. elegans*; *act-1* notably
195 compensating for *act-2* loss or for missense variants associated with strong phenotypes
196 (homozygous lethal), as shown in other studies[18,19].

197 With respect to fertility and embryonic lethality, the *act-2*(*ok1229)* allele was described as
198 thermosensitive, showing some limited embryonic lethality at 26°C (12/515 embryos, *ie* 2.3 %

199 compared to WT 3/478, *ie* 0.8%) but none observed at 15°C[29]. Therefore, we monitored the brood
200 sizes and percentage of unhatched eggs of *act-2(rey021)* at different temperatures, as well as for
201 WT and *act-2(ok1229)* animals. We observed a reduction in the number of eggs produced by the
202 *act-2*(*ok1229)* and *act-2*(*rey021)* strains compared to the WT reference both at low and high
203 temperatures (15°C and 25°C, Figure 2B). The *rey021* KO allele exhibited a high percentage of
204 unhatched eggs - above 50% - for both temperatures (Figure 2C). However, we did not detect a
205 significant decrease in embryonic development success, in contrast with the previous description
206 of the *act-2(ok1229)* (Figure 2C)[29]. For all tested conditions, we made use of Bayesian methods
207 to infer the 95% credibility intervals of the posterior distributions of the embryonic lethality rates
208 using our data set and both non-informative or informative priors. As shown (Figure 2C), *act-*
209 *2(rey021)* credibility intervals are clearly separated from that of WT, while this is not the case for
210 *act-2(ok1229)*. Thus, these results established a difference in the developmental success of the
211 different *act-2* KO alleles, the *act-2(ok1229)* allele showing a milder phenotype. As brood sizes
212 and embryonic lethality were similar for the *act-2(rey021)* at both temperatures, we did not see
213 evidence of thermosensitivity for this allele. Thus, all further experiments were performed at the
214 standard 20°C temperature.

215 To determine if the KO allele effect was dominant or recessive, we quantified brood size and
216 embryonic lethality from heterozygotes hermaphrodites for two CRISPR-generated strains.
217 Overall, the progeny of *act-2* KO animals were reduced compared to WT but *rey021*/+ animals
218 showed a higher progeny number compared to *rey021*/*rey021* (Figure 2D). This effect was not
219 observed for *rey016/*+ hermaphrodites, brood size being similar to the homozygous *rey016*
220 condition. Both progenies of heterozygous *rey021/*+ and *rey016*/+ hermaphrodites showed an
221 embryonic viability more similar to that of WT (Figure 2E, for example the median embryonic
222 lethality is 3% for the mixed progeny of *rey021*/+ hermaphrodites compared to respectively 45%
223 for *rey021*/*rey021* hermaphrodites and 0.8% for WT hermaphrodites). Taken together, both
224 *rey016* and *rey021 act-2* KO are severely impaired both in terms of fertility and embryonic lethality,
225 this phenotype is only partially suppressed in the heterozygous condition and could therefore be
226 considered as semi-dominant.

227

228 ***Reproductive capacity is a quantitative readout to classify actin mutants***

229 Assessing general animal fecundity and embryonic fitness in *C. elegans* allows for the
230 quantitative detection of potential defects in oocyte production, embryogenesis or vulva function[56],

231 three actin-dependent processes. Thus, we measured the number of eggs laid and hatched by
232 single homozygous animals expressing an *act-2* variant at 20°C. A reduction in egg laying was
233 observed for all *act-2* variants, except for the p.G74S and p.R183W variant strains, which
234 appeared unaffected (Figure 3A). The most severe reductions in fecundity were observed for the
235 p.R147S and p.T203M missense variants (mean number of eggs laid: p.R147S = 2, p.T203M =
236 31, WT = 270), surpassing the reduction seen in the *act-2* KO condition (*rey021* = 78). All other
237 missense variants showed a fecundity reduction less pronounced than the KO animals.
238 Interestingly, heterozygous animals for p.R147S and p.T203M recovered a fecundity closer to WT
239 animals, suggesting an almost complete maternal rescue (Figure S3C).

240 The number of unhatched eggs also varied significantly among actin variants with a trend
241 consistent with that of fecundity (Figure 3B). The p.R147S and p.T203M variants exhibited 100%
242 embryonic lethality when homozygous (Figure 3B), thus displaying a much stronger maternal-
243 effect lethal phenotype than the homozygous *rey021* KO allele (~41-45% embryonic lethality).
244 Mating with N2 males increased the brood sizes of homozygotes p.R147S and p.T203M without
245 rescuing embryonic lethality (Figure S3A, B). In contrast, p.R147S/+ hermaphrodites showed an
246 embryonic lethality of 17% while that of p.T203M/+ hermaphrodites fell to 3% and for *rey021*/+ to
247 4% (median values, Figure S3D). This clearly indicates that the p.R147S variant has a more
248 deleterious effect than the null allele, consistent with what has been reported in patients[13]. Note
249 that all the progeny of these heterozygote animals are pooled, thus we here assessed the lethality
250 within a mix of homozygote *act-2* variants, heterozygote and WT embryos.

251 The p.L65V missense variant also showed significant embryonic lethality (33.2%) although
252 with an increased variability**.** The p.R196H variant was affected to a significant level unlike the
253 p.R196C variant, as showed by none overlapping 95% credibility intervals of the posterior
254 distributions of the embryonic lethality rates calculated with Bayesian methods (Figure 3B). No
255 other missense variants displayed a significant impairment of embryo survival. Taken together,
256 our data suggest that p.G74S and p.R183W are not impaired in their reproductive capacity;
257 p.R147S and p.T203M display a fully penetrant maternal-effect lethal phenotype; while the other
258 studied variants have much lower penetrance: a mildly decrease in fertility, associated in most
259 cases with embryo viability comparable to WT.

260

261 ***Gonad internal architecture is impaired in selected mutants***

262 As we observed an impairment in the reproductive capacity of the actin mutant strains, we
263 investigated whether these defects were associated with abnormal organization in the *C. elegans*
264 reproductive system. We performed a detailed analysis of gonad morphology by spinning-disk
265 confocal microscopy using strains expressing both an actin filament probe
266 (mex5p::Lifeact::mKate2), and endogenously labelled non-muscle myosin molecular motors
267 (NMY-2::GFP). *C. elegans* adult hermaphrodites possess two mirror-image symmetric syncytial
268 gonads shaped by highly organized actin structures. These structures include a connected
269 cytoplasm-filled core, called the rachis, surrounded by germ cells with openings facing the rachis
270 and shaped by stable actomyosin rings (Figure 3C). These rings originate from incomplete
271 cytokinesis of primordial germ cells forming the typical specific honeycomb architecture in the
272 functional adult gonad[57]. We first characterized the gonad morphology by measuring gonad and
273 rachis sizes (Figure 3D). In this analysis, the p.L65V variant presented strikingly lower values,
274 whereas the p.T203M showed a more moderate reduction. Interestingly, the variant p.G74S
275 presented higher rachis/gonad ratio than the control even though this is not correlated with a
276 perturbation of fertility. Other variants had values more similar to the WT strain but exhibited
277 greater variances. Second, we quantified defects using established criteria[58] (Figure 3E).
278 Correlated with the strong decrease of rachis size, the most pronounced phenotypes are found in
279 p.L65V animals, notably illustrated by the presence of 80% of degenerated gonads devoid of
280 oocytes or early embryos. This suggests severe impairment in gonad morphogenesis and/or
281 maintenance in these animals. Still, the penetrance was not 100% as 1 out of 5 p.L65V animals
282 harboured a normal looking gonad, which explains the viability of the strain. Other noticeable
283 phenotypes present in animals expressing different missense variants were: the presence of
284 multinucleated oocytes in 20% of p.T203M and in 11% p.T120I animals; as well as multinucleated
285 germ cells in p.T203M (100%), p.T120I (33%) and p.G74V (25%). Altogether, *act-2* variants are
286 thus associated with abnormal gonad internal organization and multinucleated germ cells, thereby
287 causing a reduction in the number of viable oocytes thus reducing progeny numbers. Lastly, *act-*
288 *2* could be required for sperm generation or function, as mating WT males to homozygous animals
289 for p.R147S and p.T203M partially rescued the drop of fecundity without improving embryonic
290 viability (Fig S3C, D). To conclude, impaired gametogenesis might explain a reduction in brood
291 size in actin variant genetic backgrounds.

292

293 ***ACT-2 variants fail at different embryogenesis stages***

294 We next sought to determine causes of the observed embryonic lethality. To this end, we
295 quantified the precise stage at which embryonic lethality occurs in the actin-mutant strains[59,60] as
296 well as eggshell shape by measuring their aspect ratios and 2D areas (Figure S3C, D). To do so,
297 we monitored the entire duration of embryogenesis using time-lapse transmitted light video-
298 microscopy (Figure 3F). Given the high variability in defects penetrance, high throughput was
299 favoured at the expense of image quality (see Methods). In line with the previous embryonic
300 lethality counts, we detected a variable proportion of *act-2* mutant embryos unable to hatch
301 (Figure 3F). Embryonic defects were categorized into various classes: (1) in the one-cell stage,
302 due to a failure to complete cell division (orange); (2) developmental arrest during gastrulation
303 (yellow), a key event involving cell shape changes and migration, highly dependent on Arp2/3
304 actin networks[61,62]; (3) developmental arrest at later steps of development (three shades of
305 purple). Class (3) was including most cases of defects and can be further subdivided into: (3i)
306 arrest during ventral enclosure (light purple), a process also known to rely on both protrusive and
307 contractile actin-related events[63]; (3ii) arrest during elongation, also referred to as Pat embryos
308 (for paralyzed at two-fold, purple), suggesting muscle-defective embryos and/or defective
309 hemidesmosomes; and (3iii) rupturing embryos during elongation, an obvious sign of impairment
310 of tissue mechanics (dark purple)[64]. Interestingly, the total percentage of defects and their
311 frequencies varied among the different genotypes but the KO condition showed a high proportion
312 of lethality in each. In contrast, homozygous p.R147S embryos suffered severely from early
313 embryonic death (cytokinesis and gastrulation defects) while for heterozygous p.R147S embryos,
314 early death was reduced and they tended to die more frequently during ventral enclosure or in
315 later stages of elongation. As elongation requires efficient muscle contractions, this result
316 corroborated the p.R147S impaired muscular capacity measured in the motility assay (Figure 5A,
317 see below). The few embryos expressing the p.T203M allele, arrested at different stages of
318 morphogenesis between gastrulation and elongation with different ratios depending on the
319 genetic condition. These findings suggest that the p.R147S and p.T203M, both in homozygote
320 and heterozygote embryos, are more detrimental or toxic for early embryogenesis than the
321 complete or partial absence of ACT-2 protein (*rey021* condition), supporting a presumptive semi-
322 dominant effect. To conclude, this analysis revealed variant-specific differences in the
323 mechanisms leading to actin-related lethality, likely associated with fine-tuning of specific actin
324 organization, dynamics or mechanoproperties in key stages of embryogenesis.

325

326 ***Altered cell mechanics but surprisingly mild cortical actin disorganization in early embryos of***
327 ***several act-2 variants***

328 We then asked whether defects emanate from abnormal cytoskeletal organization or
329 impaired force production, such as abnormal cytoskeletal contractility linked to actin-myosin
330 interaction. These possibilities are not mutually exclusive and could be linked, as architectural
331 defects can impair contractility[65]. We thus increased the time and scale resolution by performing
332 spinning-disk confocal microscopy on strains carrying the Lifeact probe to follow actin filament
333 organization as well as an endogenously labelled non-muscle myosin (NMY-2::GFP) to assess
334 contractility during the first cell divisions of *C. elegans*[66].

335 With respect to cortical architecture and dynamics, we were surprised by the normal general
336 organization of the actin networks observed in some *act-2* variants (Figure 4A), even though
337 reduced polymerization capacities have been quantified biochemically using purified proteins as
338 for p.R196H[22] or p.T120I and p.T203M[13]. Visual inspection did not reveal major signs of impaired
339 actin density or general organization in most embryos. For a few embryos, we did observe lower
340 density regions or holes in the cortex as for some p.T203M and p.L65V embryos (Figure 4A).
341 Similarly, we did not detect signs of impairment in the reproducible sequence of events taking
342 place in zygotes for most embryos. These events, which highly depend on proper cortical
343 organization and contractility, include polarity establishment associated with cortical flows,
344 pseudo-cleavage formation, and the maintenance phase where polarity is stably maintained[67,68].
345 This was evidenced by the unchanged size of the AB daughter cell in *act-2* variant conditions
346 (Figure S4). It is possible that many NMA actin variants can copolymerize with WT actin, resulting
347 in mild phenotypes of disorganization that are still compatible with life in both humans and *C.*
348 *elegans.*

349 Although most cells maintain seemingly normal actin cortical networks, we observed some
350 cell-scale defects, revealing impaired cytoskeletal properties in some embryos (Figure 4B, C, D,
351 E, F). As expected from previous analyses, we identified cell-division defects where ingression
352 progresses smoothly but subsequently retracts (Figure 4B). This suggests that cytokinesis-ring
353 assembly and contractility might not be impaired, but rather that failure happens at the last steps
354 of cytokinesis completion during abscission. We also observed a supernumerary nucleus present
355 either in the AB cell or in the P0 zygote, possibly caused by cytokinesis failure in germ cells or
356 meiosis defects due to incomplete polar body extrusion in the oocyte (Figure 4C). As meiosis and
357 cytokinesis completion share common mechanical principles linked to actin, such as the formation
358 of a contractile actin ring required to bring together closing membrane domains[69,70], these failures

359 may share a similar origin. In addition, we noticed the presence of blebs in some embryos (Figure
360 4D, E), note that blebs were also reported for two previously described *act-2* missense variants
361 the *or621* and *or295* alleles[29]. Blebs are transient cell protrusions that can be triggered by two
362 main events: the detachment of the cortex from the plasma membrane or the formation of a crack
363 in the cortex. Blebs then grow due to the internal hydrostatic pressure imposed by cortical
364 contractility[71]. Blebs were mostly observed at the 2-cell stage, at the interface between the AB
365 and P1 cells before cell rounding prior to division. We observed larger blebs, mostly in p.L65V,
366 p.T120I and p.T203M variants, emanating from AB, sometimes dragging the nucleus into the
367 bleb, before a fast retraction period. Retraction coincided with the increase of myosin at the cortex
368 at cytokinesis onset. Embryos presenting the blebbing phenotype also had transiently abnormal
369 cell shapes, an overall less round, wavier cortical surface (Figure 4D) and seemingly diminished
370 cell-cell contacts, particularly between P1 and ABp cells at the 4-cell stage. This phenotype
371 resembles cortical blebs that were proposed to reposition the cytokinesis ring of the zygote in *ani-*
372 *1(RNAi);pig-1(gm344)* embryos in the presence of excessive myosin accumulation at the anterior
373 cortex[72]. While we did not observe mispositioning of the furrow or abnormal nuclei migration, the
374 similar phenotype suggests a shared site of cortical instability.

375

376 ***Motility is mildly impaired for a few act-2 variants***

377 Like its actin cytoplasmic paralogues, ACT-2 protein is also required in muscle cells[29],
378 evidenced by dominant mutations in *act-2* impacting *C. elegans* motility, with uncoordinated (Unc)
379 phenotypes on 2D surfaces[32]. As no such strong Unc phenotype was observed in the studied *act-*
380 *2* mutants, we quantified their capacity to migrate inside a pluronic gel towards a chemoattractant
381 (food source) in a 3D burrowing assay[73]. We observed that 82.4% of WT animals and 50.2% of
382 mobility-deficient control animals (*unc-2*(*gk366*)) reached the food after 2 hours (Figure 5A). We
383 detected altered 3D migration for the KO *rey021* and for the variants p.T120I, p.R183W, p.R196C,
384 p.R196H and p.T203M, while other variants showed unaffected migration (p.L65V, p.G74S,
385 p.R147S). We verified that these effects were not due to impaired chemosensation (Figure S5).
386 Note that in this assay we observed an increased number of immobile animals for variants *rey021*
387 and p.T203M only. In conclusion, six out of nine assessed *act-2* variants have impaired 3D
388 motility, while two variants display a substantial percentage of animals that are defective both for
389 2D and 3D movement.

390

391 ***Low penetrance of neurogenesis defects***

392 In humans, neurodevelopmental defects are the most frequent symptoms across the NMA
393 spectrum. We thus studied neurons in *C. elegans* L4 animals. To this aim, we took advantage of
394 a multicolour neuronal labelling transgene present in the NeuroPAL strain[74]. The NeuroPAL
395 transgene codes for the expression of a combination of 41 neuron specific reporters for gene
396 expression and neuronal activity, associated with four different fluorophores. This labelling allows
397 each neuron in the animal to be identified by a unique set of fluorophores, distinguishing them
398 from neighbouring neurons. After introducing the NeuroPAL transgene in the actin variant strains,
399 we mapped all neurons present in the animal's midbody and tail, which include every type of
400 neuron. For every observed animal, we did not detect altered neuronal positions. However, we
401 did observe rare events, for each allele except p.R196H, wherein we detected the presence of a
402 supernumerary neuron (adjacent to SDQR or in the lumbar ganglion) or a missing neuron (such
403 as DVB or PDA, Figure 5C). These altered numbers suggest that NMA neurodevelopment defects
404 may be reproduced in our mutant models.

405

406 ***Data integration to build a comparative tool***

407 Taking advantage of the multiscale characterization performed on each mutant, our final goal
408 was to classify the different missense variants in terms of severity. We used each of the
409 quantitative results as variables to create a Principal Component Analysis (PCA) graphical
410 representation (Figure 6, variables available in Figure S6). This dimension reduction allowed us
411 to group phenotypes into different classes and allowed us to identify the few most promising
412 variables to be used for classification purposes (Figure S6). In the PCA plot, the WT strain was
413 located in the left side close to the mildly affected variants (p.G74S, p.T120I, p.R183W, p.R196C,
414 p.R196H), thus defining class I: characterized by negative values along dimension 1. One can
415 note the singular position of the p.L65V, isolated at the boundary of the class I group, emphasizing
416 some specificity with respects to this variant. This result correlated with human data, where an
417 *ACTB* p.L65V patient presented severe symptoms and early death. The KO *rey021* strain was
418 also isolated in a more central position. Stronger phenotypes such as in p.R147S or p.T203M
419 variants were positioned in the right half, defining class II (positive values along dimension 1).
420 Euclidian distances calculated between each variant and the wild type reference confirmed the
421 choice of groups: class I variants were grouped bellow a distance of 3 and class II positioned
422 above this threshold (Figure 6B). Interestingly, heterozygous variants (*rey021*/+, p.R147S/+ and
423 p.T203M/+*)* were positioned closer to the WT than their homozygous counterparts, thus in

424 accordance with a reduction of the severity of the defects in presence of one wild-type *act-2* allele.
425 Differences in the directionality of these repositioning trajectories probably underly differences in
426 the mechanism at the origin of the defects that may affect differently the scored phenotypes
427 (Figure S6A). To assess the robustness of our analysis we performed additional PCA either
428 removing all the data linked to the insertion of fluorescence in the *act-2* variant genetic
429 background, thus keeping the most easily quantifiable phenotypes (Figure S6C, D) or removing
430 the two most lethal strains p.R147S and p.T203M (Figure S6E, F). The similarity of the PCA 6B
431 and S6C showed that the removal of these specific variables did not modify the overall positioning
432 of strains, whereas the PCA S6E confirms the respective positioning of the homozygous variants
433 for example, p.L65V notably clearly apart from WT and other *act-2* variant studied. In conclusion,
434 using quantitative multiscale analysis of a panel of actin variants, we have provided access to a
435 valuable comparative tool enabling the positioning of newly identified variants on a graded map
436 of survival potential, if such new variants were obtained and analysed using the same parameters
437 reflected in our PCA analysis.

438

439 **DISCUSSION**

440 Patients affected by the rare disorders from the Non-Muscle Actinopathies (NMA) spectrum
441 and its subclass BWCFF, exhibit a large range of symptoms and diverse survival potential, leading
442 to complicated medical prognostics. Given the ubiquitous nature of actin, which is involved in
443 numerous cellular events at all stages of development and throughout lifespan, it is important to
444 analyse multiple phenotypic parameters in animal models. Ideally in order to effectively distinguish
445 the impact of each actin variant, these parameters should span diverse length scales: from
446 macroscopic actin organisation to cell behaviours and phenotypes at the organism scale. In this
447 study, we used the fast-growing and simple model organism *C. elegans* to study *in vivo* the
448 quantitative impact of some of the associated single cytoplasmic actin variants. Using
449 CRISPR/Cas9 genome editing, we successfully generated new *C. elegans* models expressing
450 endogenously either *de novo* actin variants identified in human patients or premature STOP
451 mutations to reproduce loss-of-function conditions. For each variant, we quantified general
452 fitness, reproductive capacities, muscle-based motility, embryonic development, and neuronal
453 differentiation. The final step using an integrated PCA analysis enabled us to summarize the
454 phenotypic classification, providing a valuable tool to position newly identified variants of unknown
455 significance on an existing map. We foresee that these data support the use of *C. elegans act-2*
456 mutations as a pertinent and promising model for the investigation of NMA.

457 A key finding of the functional characterization of *act-2*, was the significant phenotypic
458 difference between different *act-2* knock-out strains *(rey021, rey016, ok1229).* In summary no
459 *act-2* mRNA was detected for allele *act-2(rey021) and act-2(ok1229)* but an upregulation of *act-*
460 *1* mRNA levels was clearly observed only for *act-2(rey021)*. Regarding fertility, brood sizes were
461 reduced in all homozygous KO conditions but were variable in the heterozygote *rey021/*+ and
462 rey016/+ conditions (partially improved only in the *rey021/*+ condition). Regarding embryonic
463 lethality, the phenotypic differences between alleles were even more pronounced: it varied from
464 no embryonic lethality for *act-2(ok1229)* to different penetrance of lethality for *rey016* and *rey021*
465 that were strongly but not fully rescued in heterozygote maternal conditions. Therefore, the *act-*
466 *2(rey021)* and *act-2(rey016)* alleles showed a semi-dominant effect as they are not fully rescued
467 in the heterozygote condition. To conclude, we suspect that these alleles are haplo-insufficient,
468 with both a maternal and zygotic effect, unlike *act-2(ok1229)* that was associated with reduced
469 brood sizes but presented a comparable embryonic lethality as wild-type. Such a difference
470 among the KO strains was unexpected and we can only hypothesize on its origin: it could probably
471 be linked to the presence of different and intricate mechanisms allowing to sustain actin
472 homeostasis compensating its loss. These mechanisms include genetic compensation also
473 referred to as isoactin switching, dosage compensation and transcriptional adaptation.
474 Additionally, the presence of different feedback mechanisms either relying on the gene locus,
475 mRNA, or the actin protein itself, may be at work differentially in these genetic contexts[26]. The
476 absence of major changes in other actin expression levels for some missense variants (L65V,
477 R196H, R196H) but presence of changes for more deleterious missense variants (R147S,
478 T203M) reinforces the possibility that different levels of regulation may be at play. Note that
479 different compensation efficiencies may vary both between embryo and L4 animals and may have
480 some tissue specificity.

481 For *ok1229*, it is also possible that a linked non-identified second-site modifier (eg. a linked
482 suppressor mutation) was introduced during non-targeted mutagenesis, resulting in the observed
483 differences with the CRISPR-generated alleles. As in human where loss of a cytoplasmic actin
484 allele induces a compensatory transcriptional adaptation[7,24,25,75], *C. elegans* showed
485 transcriptional adaptation to compensate for *act-2* loss, as the closely related actin paralogue
486 gene *act-1* was found to be upregulated in the *rey021* condition. One hypothesis for the absence
487 of compensation in other conditions, could be the loss of a 25bp key sequence located in *act-2*
488 second intron that was shown to both regulate actin genes expression and be required for
489 transcriptional adaptation[18,19], or loss of another regulatory element in the deleted regions of
490 *ok1229* or *rey016*. This sequence is indeed removed both in *rey016* and *ok1229* but not in *rey021*

491 in which it may still act to induce an overexpression of *act-1* via mRNA-linked transcriptional
492 adaptation. Note that no significative change was observed in *act-3* levels in these contexts.

493 Beyond regulation via paralogue gene expression, actin levels are additionally regulated at
494 posttranscriptional and posttranslational levels and actin concentration was also shown to
495 regulate actin mRNA synthesis, all these effects are possibly differentially affecting cytoplasmic
496 actin concentrations in these genetic contexts[76,77]. Overall, this shows that a fine tuning of the
497 actin abundance is at work and impacting the different function we assessed, and that the
498 presence of ACT-2 is notably important for maintaining a high fertility and ensuring the success
499 of embryonic development.

500 Another significant finding was that three actin variants exhibited stronger phenotypes than
501 the *rey021 act-2* KO, namely p.G74V, p.T203M and p.R147S. The p.G74V variant led to animals
502 producing 100% lethal embryos even when heterozygote, therefore harbouring a strong dominant
503 maternal-effect lethal phenotype. In contrast, embryos from variants p.T203M and p.R147S were
504 100% lethal only when the mother was homozygous, showing a fully penetrant maternal-effect
505 lethal phenotype, with a stronger effect than that of null alleles. However, the latter mutations
506 were strongly improved in heterozygotes animals to a comparable extent than the *rey021/+*
507 condition. Still, especially for the p.R147S missense variant, heterozygous animals displayed a
508 low embryonic lethality consistent with a semi-dominant allelic effect. This could indicate that the
509 presence of this mutated actin residue disrupts proper cytoskeletal function, either through
510 essential perturbations of actin filament assembly or by interactions with actin-binding proteins.
511 These two variants p.G74V, p.R147S and possibly p.T203M could act as semi-dominant negative
512 alleles by antagonising normal polymerisation kinetics of the wild-type actin and thus affecting a
513 diversity of cellular function notably required for the success of embryonic development. To
514 distinguish dominant negative effect from other gain-of-function mechanisms, one could test if
515 increasing amount of wild-type protein is enough to rescue the lethality. At the biochemistry level,
516 a simplification considering actin polymerisation kinetics in isolation, such hypothesis could be
517 easily tested using a range of protein concentrations[20,22,50]. However, actin polymerisation is just
518 one of the many parameters of actin *in vivo* role and is probably not sufficient to explain
519 phenotypes of more complex *in vivo* situations. Indeed, if both p.R196H and p.T203M have
520 impaired *in vitro* polymerisation rates, only p.T203M allele is severely impacting *C. elegans* fitness
521 and embryonic success. Thus, the combination of both findings, *in vitro* biochemistry and *in vivo*
522 animal models, provides key information to determine the impact of each actin variant.

523 Using these models, we observed an unexpected striking difference between two
524 substitutions at the same residue. Animals expressing the p.G74S variant show only mild effects
525 on embryonic viability whereas the p.G74V animals are significantly more affected, as mentioned
526 above. This position is of particular interest because of the neighbouring His73 which is known to
527 undergo irreversible methylation, regulating actin's interdomain flexibility in multiple species and
528 known to affect smooth muscle contraction in mice for example[50,78]. Additionally, due to its location
529 within the nucleotide-binding cleft, this variant might impact the phosphate release following actin
530 monomer incorporation into the filament. Consequently, the binding of ADF/cofilin would be
531 perturbed, leading to impaired disassembly kinetics. Of note, *C. elegans'* ADF/cofilin homologue
532 UNC-60 induces lethality when knocked down[79]. Biochemical analysis and *in vitro* studies using
533 purified actin variants could examine these hypotheses and compare biochemically how the
534 presence of the hydrophobic Valine is more detrimental than Serine.

535 Additionally, and from a more fundamental perspective, characterizing actin variants is also
536 powerful to reveal new properties of actin networks. The observed abnormal internal gonad
537 organization is highlighting the importance of ACT-2 for proper cytoskeleton architecture
538 establishment in this tissue. The presence of multinucleated cells revealed the importance of
539 ACT-2 in cytokinesis and possibly meiosis. Blebs, on the other hand, are intrinsically linked to
540 cortical contractility and to cortex-to-membrane attachment, thus reinforcing the possibility that
541 membrane-to-cortex attachment might be impaired, as also suggested by late cytokinesis defects.
542 We use this rationale to propose that variant p.L65V is detrimental to gonad cytoskeleton
543 organisation and functional oocyte production; p.R147S possibly impairs mostly branched actin
544 networks essential at different morphogenesis stages; and p.T203M, p.T120I, and p.R196C/H
545 impact contractility as indicated by blebbing, paralysed arrest and impaired motility. As we have
546 demonstrated that developmental arrest at critical embryonic stages occurs at varying frequencies
547 depending on the nature of the variant or copy number —in the case of p.R147S— we propose
548 that these key developmental stages act as specific "barriers" to developmental success, barriers
549 of different difficulty linked to the precise site of mutation, that must be successively overcome
550 during embryogenesis. As developmental timings[80] were not drastically affected (Figure S3G), we
551 suspect that these barriers might have a biomechanical origin. Alternatively, it is possible that
552 some stochastic defects in the early embryo such as lineage defects or mispositioning of cells
553 could lead to developmental arrest at later cell stages. A recent study by Xiao and colleagues[81]
554 sheds light on how cellular plasticity can buffer genetically-induced defects in *C. elegans* embryos.
555 Thus, another hypothesis would be that our variants do not only impair morphogenesis per say -
556 at the observed timing of arrest- but might be resulting from earlier defects which could have been

557 initially compensated. A more detailed analysis of early embryonic development, such as using
558 automated profiling of embryonic development[82,83] or lineage tracing methods[84] could enable to
559 verify such hypothesis.

560 Observed defects commonly display incomplete penetrance and the general organization of
561 actin at a macroscopic scale is often remarkably unaffected. This suggests an adaptation of
562 cytoskeletal actin to perturbations, possibly originating from the cell's ability to maintain the
563 adequate large-scale physical properties of the cortex, also known as “morphogenetic
564 degeneracies in the actomyosin cortex”[85]. Compensation mechanisms may ensure the
565 robustness of embryonic development by maintaining proper cytoskeleton mechanical properties.
566 Note that a similar robustness to cytoskeletal perturbation, in that case a resistance to microtubule
567 disassembly, was observed in the context of *C. elegans* embryonic elongation[86,87]. In the context
568 of actin, this could also be explained by a functional compensation by other actin isotypes
569 expressed in early embryogenesis, notably ACT-1 or ACT-3, which might compensate for
570 polymerization defects. *In vitro* experiments with purified proteins using mixtures of WT and
571 mutant actin, such as p.R196H, also show a partial rescue of polymerization defects[22]. Thus,
572 biological variations such as gene expression fluctuation, gene compensation, actin and ABP
573 concentrations, mechanochemical feedback or fluctuation of properties impacting cell or tissue
574 mechanics, determine the success of embryogenesis for each individual. Consequently, each
575 embryo may respond differently to these compensation mechanisms and might arrest at a
576 different developmental stage. In order to go a step further, a detailed analysis of actin spatio-
577 temporal organisation and actin molecular dynamics together with the study of some key actin
578 binding proteins such as myosin, formin or capping-protein both in the early embryo as well as
579 during some key stages of development, will enable to reveal additional details on the respective
580 molecular effects of these actin variants in a living animal.

581 Finally, the initial investigation of the consequences of actin perturbation on neurogenesis
582 revealed a defect in acquiring the correct number of neurons, albeit not penetrant. SDQ neurons
583 are born from an asymmetric division followed by the death of their sister cell while DVB and PDA
584 are born from the trans-differentiation of a rectal epithelial cell[88]. Even at low penetrance, these
585 numbers are notable, due to the 100% invariance of these neuronal lineages in *C. elegans* under
586 wild-type conditions[88,89]. These findings suggest a potential defect in the process of neuronal
587 asymmetric division or fate acquisition, which might be amplified in the context of human cortical
588 development where neuron numbers are far greater and asymmetric divisions have been reported
589 in the striatum. The asymmetric divisions required for neuronal fate acquisition can depend on

590 the asymmetry of Arp2/3 nucleated cortical actin polymerisation[89]. As both actin polymerisation
591 and Arp2/3 nucleation were already described to be impaired for some variants studied *in vitro*[22],
592 this result is not surprising and will require further investigation in *C. elegans*. Such additional
593 studies may lead to advances in identifying the links between the molecular and functional levels
594 that underlie NMA neuronal pathophysiology. Importantly, the NeuroPAL data using nuclei as
595 proxy of neuronal cell positioning, did not reveal other gross defects in terms of cell migration.
596 This might be due to the redundancy at work during development that ensures the robustness of
597 final neuronal positioning in *C. elegans*. Assessing migration dynamics and axonal networks may
598 uncover additional abnormalities not visible in the current analysis.

599 As all animal models, the use of *act-2* variants in *C. elegans* has some limitation. First of all,
600 we do not have a confirmed correspondence between the three *C. elegans* cytoplasmic actin
601 paralogues and the human *ACTB* or *ACTG1* genes. Even if ubiquitous, the *act-2* expression may
602 vary in abundance in *C. elegans* cells or tissues compared to the two human cytoplasmic actin,
603 thus introducing possible bias or misinterpretations. For instance, the key role of ACT-2 for proper
604 gonad organization and fertility might be specific to *C. elegans* and might not have a direct
605 equivalent in human. We however think that the highly conserved *in vivo* actin-related
606 biochemistry is ensuring, notably in the case of strong perturbation, that variants identified as
607 inducing strong perturbation in *C. elegans* also have a negative impact in human cells.

608 Altogether, this work provides a new animal-model library for the study of actin variants
609 associated with NMA. We show that different non-synonymous mutations in nematodes lead to a
610 broad range of phenotypes as in humans, and that the severity of *C. elegans* phenotypes
611 correlates with patients' survival potential. For example, two severely affected *C. elegans* strains
612 are p.R147S and p.T203M. This correlates with the observation that several *ACTB* p.R147S
613 patients were identified harbouring only post-zygotic mutations, thus expressed as mosaics in a
614 subset of epithelial cells suggesting a lethal issue in human if expressed in all cells[40]. Additionally,
615 several patients with variant p.T203M in *ACTG1* suffer from severe BWCFF symptoms including
616 microcephaly, profound intellectual disability and non-ambulance[13]. This residue is known to be
617 a hot spot for *ACTG1* but no patient with an *ACTB* mutation has been identified so far, raising the
618 question of lethality for *ACTB* in humans. Similarly, the *C. elegans* variant p.G74V showed 100%
619 lethality and patients with p.G74V variant in *ACTG1* are severely affected, while no *ACTB* p.G74V
620 variant has been discovered so far. To conclude, the severity of this initial set of *C. elegans*
621 mutants correlates with that reported in human patients.

With commercial gene editing services in *C. elegans* offering quick delivery times and automated analysis of various criteria, it is plausible that *C. elegans* NMA models may be used in the future as indicators to aid clinical prognosis for humans. Additionally, all the tools generated here could be used to investigate further the mechanisms underlying NMA pathophysiology, including genetic suppressor screens and/or drug screening for therapeutic strategies.

Limitations of the study

In our opinion, this study has three major limitations. As the correspondence between the *C. elegans* cytoplasmic actin orthologues and the human ACTB or ACTG1 genes is still unknown, we used *act-2* to model variants of both types. All three proteins are highly similar and the most probable cause of the identified functional differences between ACTB and ACTG1 possibly lies in their genetic encoding[15,23]. Consequently, even if ubiquitous, *act-2* expression may vary in abundance in *C. elegans* cells or tissues compared to the two human cytoplasmic actins, thus introducing possible bias or misinterpretations. Second, we report strikingly different phenotypes for different null alleles in the *C. elegans act-2* gene: the *ok1229* allele showed a very moderate phenotype in contrast to the *rey021* or *rey016* alleles. Although null alleles are expected to induce similar phenotypes, several possibilities may explain this discrepancy, notably the presence of variable compensation of actin proteins (also see the discussion). In addition to the observed rescue of embryonic lethality in heterozygotes (*rey021/+* or *rey016/+),* to further address this issue, a rescue experiment with a wild-type version of an *act-2* transgene could have been performed to rule out the existence of potential linked mutation(s) causing the phenotype. Third, concerning gene compensation between actin genes, we must admit that our RT-qPCR experiments showed a high variability, likely arising from a biological source as technical replicates were more alike. Given that these experiments were performed on individual animals, it is possible that this variability may come from differences in the level of genetic compensation at work in the selected animals.

RESOURCE AVAILABILITY

Lead contact

Requests for further information and resources should be directed to and will be fulfilled by the lead contact, Anne-Cécile Reymann (reymanna@igbmc.fr).

Materials availability

All generated *C. elegans* strains generated in this study are available from the lead contact -if not already available at the *Caenorhabditis* Genetics Center (CGC).

Data and code availability

Data: All data reported in this paper will be shared by the lead contact upon request.

Code: All original code has been deposited and is publicly available via our GitLab (https://gitlab.com/igbmc/reymannlab/2025-hecquet-iscience).

Additional information

Any additional information required to reanalyze the data reported in this paper is available from the lead contact upon request.

ACKNOWLEDGMENTS

This work was funded by European Joint Program for Rare Diseases through the European Union's Horizon 2020 research and innovation program under the EJP RD COFUND–EJP N° 825575. N.D.D. and D.J.M./J.N.G. with support from the German Federal Ministry of Education and Research under Grant Agreements 01GM1922A and 01GM1922B, respectively. A-C.R. under the project ANR-19-RAR4-0001-03. A-C.R. was also supported by the French Fondation Maladies Rares under the project SAM-2022-121409. This work of the Interdisciplinary Thematic Institute IMCBio+, as part of the ITI 2021-2028 program of the University of Strasbourg, CNRS and Inserm, was supported by IdEx Unistra (ANR-10-IDEX-0002), and by SFRI-STRAT'US project (ANR-20-SFRI-0012) and EUR IMCBio (ANR-17-EURE-0023) under the framework of the France 2030 Program. N.D.D received grant support from Deutsche Forschungsgemeischaft (DFG) (DI 2170/3-1 and DI 2170/5-1), Else-Kröner-Fresenius Stiftung (2020_EKES.04) and German Federal Ministry of Education and Research under Grant Agreements 01GM1922A. We acknowledge the Imaging Center of IGBMC, member of the national infrastructure France-BioImaging supported by the French National Research Agency (ANR-10-INBS-04). A-C.R. is a CNRS investigator. N.A. is an Unistra technician personnel. J.N.G. is supported by the HiLF I grant for early career researchers from Hannover Medical School. Some strains were also provided by the CGC, which is funded by NIH Office of Research Infrastructure Programs (P40 OD010440).

We would like to particularly thank the Imaging Center of IGBMC (ici.igbmc.fr) with the assistance of Elvire Guiot, Erwan Grandgirard, Yves Lutz and Bertrand Vernay. We warmly thank Dietmar Manstein (D.J.M) for his significant contributions to the project design and throughout grant application procedures. We also thank Juliette Godin, Michel Labouesse and Patrick Reilly for critical reading of the manuscript. We thank Robert W. Fernandez, post doc in Oliver Hobert's lab, for training us to NeuroPAL as well as our junior visitor scientists Fanny Bouvier, Emil Zessin and Johann Marois for their help.

AUTHOR CONTRIBUTIONS

Conceptualisation A-C.R., N.D.D., T.H.; Methodology A-C.R., T.H.; Investigation T.H., N.A., D.S., A.G., G.A., S.Y., F.M., S.Q., J.G., A-C.R.; Writing -Original Draft, A-C.R., T.H.; Writing -Review & Editing, A-C.R., T.H., J.G., N.D.D., S.Q.; Funding Acquisition, A-C.R., N.D.D, D.J.M, J.G.; Resources, A-C.R.; Supervision, A-C.R..

DECLARATION OF INTERESTS

The authors declare no competing interest.

701 **SUPPLEMENTAL INFORMATION**

702 Document S1. Figures S1-S6, Tables S1-S3 and supplemental references

703 Video S1. Cytokinesis arrest, p.R196C embryo. Scale bar = 10µm, related to Figure 3

704 Video S2. Gastrulation arrest, p.G74S embryo. Scale bar = 10µm, related to Figure 3

705 Video S3. Ventral enclosure arrest, *rey021* embryo. Scale bar = 10µm, related to Figure 3

706 Video S4. Extremity burst arrest, p.L65V embryo. Scale bar = 10µm, related to Figure 3

707 Video S5. Paralyzed arrest, rey021 embryo. Scale bar = 10µm, related to Figure 3

708 Video S6. Cytokinesis defects, p.R196C embryo. Lifeact::mKate2 (Magenta), NMY-2::GFP (Green). Scale
709 bar = 10µm. Anterior on the left, related to Figure 4

710 Video S7. Meiosis defects, p.R196C embryo. Lifeact::mKate2 (Magenta), NMY-2::GFP (Green). Scale bar =
711 10µm. Anterior on the left, related to Figure 4

712 Video S8. Bleb defects, p.T120I embryo. Lifeact::mKate2 (Magenta), NMY-2::GFP (Green). Scale bar =
713 10µm. Anterior on the left, related to Figure 4

714

715 ## FIGURE TITLES AND LEGENDS

716 ### Figure 1. Insertion of Non-Muscle Actinopathies variants in the *C. elegans act-2*

717 (A) Dot heatmap of patients' symptoms. Intellectual disability (ID) level letter code : n=none,
718 m=mild, mo=moderate, s=severe, p=profound. MRI = Magnetic Resonance Imaging. BWCFF =
719 Baraitser-Winter Cerebro Fronto Facial syndrome. (B) Structural model of ACT-2 G-actin
720 generated by Alphafold2. Subdomains of ACT-2 are coloured in grey (SD1), light grey (SD2), blue
721 (SD3) and light blue (SD4). (Right) Homology model of the ACT-2 filament (based on PDB-ID:
722 8DNH). ACT-2 protomers are coloured in different shades of blue. The mutated residues
723 investigated in this study are shown in red. The ATP bound to the individual protomers is shown
724 as a stick-model. The zoom-in shows the location and structural environment of the individual
725 mutated residues in more detail. (C) Schematic *act-2* representation highlighting the location of
726 single point variants obtained via CRISPR edition. Three *act-2* gene knockout alleles are also
727 depicted: *rey016*, *rey021* and *ok1229*[29]. Note that the amino acid numbering is here in frame with
728 human ACTB/ACTG1, consider -1 AA in the frame of *C. elegans* due to an additional cysteine in
729 second N-ter position, the base pair are however kept in the *C. elegans act-2* frame. (D) Table
730 summarizing the overall viability of *C. elegans act-2* variants at 20°C.

731 ### Figure 2. *act-2* gene knock-outs affects fertility despite compensation mechanisms

732 (A) Single animal RT-qPCR showing the normalized amount of mRNA for each *C. elegans*
733 actin coding genes. Normalization was done using a housekeeping gene (*iscu-1)* and WT values.
734 Different colours show different replicates. Small dot is the value for one animal while bigger dots
735 correspond to the experiment's mean. Diamonds show the mean of all replicates. (B) Progeny
736 number per homozygous *act-2* knockout (*ok1229* and *rey021*) animal, at the mentioned
737 temperatures, counted during 48h. Standardised boxplots and mean values (diamond) are shown
738 (C) Percentage of eggs that failed to hatch. The mean number of eggs that did not hatch for one
739 animal is shown as a dot or a triangle, overlaid by standardised boxplots and mean values
740 represented by a diamond. The rightmost plot presents the 95% credibility intervals of the
741 posterior distributions of the embryonic lethality rates, considering low informative priors
742 described in the methods section and our observed data set. These are calculated with a
743 Bayesian model based on Poisson laws with an offset to account for the progeny numbers.
744 Experimental values are represented by red diamonds (mean) and cyan rhombus (median). (D)
745 Progeny number at 20°C counted for 72h per homozygous or heterozygous *act-2* KO animal.
746 Standardised boxplots and mean values (diamond) are shown. (E) Percentage of eggs that failed
747 to hatch. The mean number of eggs that did not hatch for one animal is shown as a dot, overlaid
748 by standardised boxplots and mean values represented by a diamond. The rightmost plot
749 presents the 95% credibility intervals of the posterior distributions of the embryonic lethality rates
750 considering low informative priors described in the methods section and our observed data set.
751 These are calculated with a Bayesian model based on Poisson laws with an offset to account for
752 the progeny numbers. Experimental values are represented by red diamonds (mean) and cyan
753 rhombus (median). (B, C, D, E) Boxplots display the maximum and minimum values, the median
754 as well as first and third quartiles.

755

756 ### Figure 3. *act-2* variants affect egg-laying capacities and embryogenesis success

757 (A) Total progeny number at 20°C per homozygous *act-2* variant. The sum of eggs laid for
758 one animal is shown as a dot, overlaid by standardised boxplots and mean values represented

759 by a diamond. (B) Percentage of eggs that failed to hatch. The percent of dead eggs for one
760 animal is shown as a dot, overlaid by standardised boxplots and mean values represented by a
761 diamond. Boxplots display the maximum and minimum values, the median as well as first and
762 third quartiles. The rightmost plot presents the 95% credibility intervals of the posterior
763 distributions of the embryonic lethality rates considering the priors described in the methods
764 section and our observed data set. These are calculated with a Bayesian model based on Poisson
765 laws with an offset to account for the progeny numbers. Experimental values are represented by
766 red diamonds (mean) and blue circles (median). (C) Actin organization in a WT gonad observed
767 using an actin probe (Lifeact::mKate2), max projection of a Z-series of images. Green and purple
768 arrows illustrate the space measured to calculate the rachis/gonad ratio measured in front of the
769 -1 oocyte. Scale bar is 20µm. (D) Boxplot presenting the ratio between the rachis and the gonad
770 width of homozygote animals. Mean is represented as a diamond. (E) Heatmap of observed
771 phenotypes, in percent. (F) Stacked histogram of the end status of embryogenesis for different
772 *act-2* variants in percent. Schemes on the left represent the different defects observed. Also see
773 Videos S1, S2, S3, S4 and S5.

774 **Figure 4. Actin mutation effects on cortical organization in early embryos**

775 (A) Cortical plane of embryos at different stages, Lifeact::mKate2 shown in magenta and
776 NMY-2::GFP shown in green, to reveal actin filaments and myosin distribution. p.T203M animals
777 only have Lifeact::mKate2. (PN = Pronuclei) Anterior is on the left. (B, C, D) Equatorial plane
778 image of embryos expressing Lifeact::mKate2 (magenta) and NMY-2::GFP (green). (B)
779 Cytokinesis defect observed. The cytokinesis ring relaxes after completion of a first ingression
780 (pink arrow), this is followed by multiple simultaneous ingressions as the cell proceeds to divide
781 directly into four daughter cells. See Video S6. (C) An additional nucleus is visible (blue arrow).
782 Nuclei are circled. See Video S7. (D) Blebbing. Large protrusion called bleb extrude from the
783 anterior cell (orange arrow). After actin and myosin reassembly, the bleb retracted and division
784 seemed to occur normally. See Video S8. (E) Abnormal membrane ruffling is observed in some
785 embryos (white arrow). (F) Cortical plane of embryos presenting other phenotypes. Abnormal
786 aspect ratio of the cortex implies a rounder embryo (see also Figure S4). Abnormal division axis
787 (red arrows) leads to abnormal cell-cell contacts. Breaks in the cortex are highlighted by green
788 arrows. (*) Embryos from homozygote actin variants expressing Lifeact::mKate2 only. Scale bar
789 is 10µm.

790 **Figure 5. Actin mutations can affect motility and/or neuronal cell number**

791 (A) 3D animal migration assay. Percentage of animals reaching a chemoattractant after
792 migration inside a pluronic gel, monitored every 15 minutes for 2 hours. Results for individual
793 wells (N) for each variant are visible as transparent dots, n is the total number of animals assessed
794 and bars show the standard deviation. The final proportion for each variant was compared to that
795 of WT in the frame of Bayesian statistics, using two binomial distributions. The odds ratio (OR) as
796 well as the probability (p) that the difference is superior to 0.2 are indicated. (B) Variation of the
797 neuronal cell number are observed in *act-2* variant conditions. Reconstructed image of an animal
798 expressing the NeuroPal transgene. Insets show representative images of identified defects
799 compared to the WT *act-2* reference: presence of a micronucleus (Orange), an extra (Magenta)
800 or a missing cell (Green). Scale bar is 50 µm. (C) Summary of neuronal phenotypes observed in
801 the actin variants.

802 **Figure 6. Data integration to build a comparative tool**

(A) Principal Component Analysis plot of analysed actin variant animals reveal clusters which can be associated to classes of phenotypes. Corresponding table with data is available in Figure S6A. p.G74V was added manually as no data could be retrieved for this strain. Arrows link homozygotes to their respective heterozygotes. (B) Distances calculated between each actin variant and the WT reference in the two first dimensions.

809 ## REFERENCES

810

811 1. Blanchoin, L., Boujemaa-Paterski, R., Sykes, C., and Plastino, J. (2014). Actin dynamics, architecture,
812 and mechanics in cell motility. Physiol. Rev. *94*, 235–263.
813 https://doi.org/10.1152/physrev.00018.2013.

814 2. Murrell, M., Oakes, P.W., Lenz, M., and Gardel, M.L. (2015). Forcing cells into shape: the mechanics
815 of actomyosin contractility. Nat. Publ. Group *16*, 486–498.

816 3. Kruse, K., Berthoz, R., Barberi, L., Reymann, A.-C., and Riveline, D. (2024). Actomyosin clusters as
817 active units shaping living matter. Curr. Biol. CB *34*, R1045–R1058.
818 https://doi.org/10.1016/j.cub.2024.08.043.

819 4. Lappalainen, P., Kotila, T., Jégou, A., and Romet-Lemonne, G. (2022). Biochemical and mechanical
820 regulation of actin dynamics. Nat. Rev. Mol. Cell Biol. *23*, 836–852. https://doi.org/10.1038/s41580-
821 022-00508-4.

822 5. Parker, F., Baboolal, T.G., and Peckham, M. (2020). Actin Mutations and Their Role in Disease. Int. J.
823 Mol. Sci. *21*, 3371. https://doi.org/10.3390/ijms21093371.

824 6. Lai, W.-F., and Wong, W.-T. (2020). Roles of the actin cytoskeleton in aging and age-associated
825 diseases. Ageing Res. Rev. *58*, 101021. https://doi.org/10.1016/j.arr.2020.101021.

826 7. Cuvertino, S., Stuart, H.M., Chandler, K.E., Roberts, N.A., Armstrong, R., Bernardini, L., Bhaskar, S.,
827 Callewaert, B., Clayton-Smith, J., Davalillo, C.H., et al. (2017). ACTB Loss-of-Function Mutations
828 Result in a Pleiotropic Developmental Disorder. Am. J. Hum. Genet. *101*, 1021–1033.

829 8. Latham, S.L., Ehmke, N., Reinke, P.Y.A., Taft, M.H., Eicke, D., Reindl, T., Stenzel, W., Lyons, M.J.,
830 Friez, M.J., Lee, J.A., et al. (2018). Variants in exons 5 and 6 of ACTB cause syndromic
831 thrombocytopenia. Nat. Commun. *9*, 4250. https://doi.org/10.1038/s41467-018-06713-0.

832 9. Polubothu, S., Abdin, D., Barysch, M., Thomas, A., Bulstrode, N., Evans, R., Solman, L., Obwegeser, J.,
833 Hennekam, R.C., Weibel, L., et al. (2020). Dermatological signs lead to discovery of mosaic ACTB
834 variants in segmental odontomaxillary dysplasia. Br. J. Dermatol. *183*, 1128–1130.
835 https://doi.org/10.1111/bjd.19339.

836 10. Rivière, J.-B., Van Bon, B.W.M., Hoischen, A., Kholmanskikh, S.S., O'Roak, B.J., Gilissen, C., Gijsen, S.,
837 Sullivan, C.T., Christian, S.L., Abdul-Rahman, O.A., et al. (2012). De novo mutations in the actin genes
838 ACTB and ACTG1 cause Baraitser-Winter syndrome. Nat. Genet. *44*, 440–444.
839 https://doi.org/10.1038/ng.1091.

840 11. Verloes, A., Di Donato, N., Masliah-Planchon, J., Jongmans, M., Abdul-Raman, O.A., Albrecht, B.,
841 Allanson, J., Brunner, H., Bertola, D., Chassaing, N., et al. (2015). Baraitser–Winter
842 cerebrofrontofacial syndrome: delineation of the spectrum in 42 cases. Eur. J. Hum. Genet. *23*, 292–
843 301. https://doi.org/10.1038/ejhg.2014.95.

12. Verloes, A., Drunat, S., Pilz, D., and Di Donato, N. (1993). Baraitser-Winter Cerebrofrontofacial Syndrome. In GeneReviews®, M. P. Adam, J. Feldman, G. M. Mirzaa, R. A. Pagon, S. E. Wallace, L. J. Bean, K. W. Gripp, and A. Amemiya, eds. (University of Washington, Seattle).

13. Donato, N.D., Consortium, N.M.A., Thom, A., Rump, A., Greve, J.N., Kropp, M., Cadiñanos, J., Calabro, S., Cathey, S., Chung, B., et al. (2024). Genomic and biological panoramas of non-muscle actinopathies. Preprint at medRxiv, https://doi.org/10.1101/2024.08.21.24310320 https://doi.org/10.1101/2024.08.21.24310320.

14. Dugina, V., Zwaenepoel, I., Gabbiani, G., Clément, S., and Chaponnier, C. (2009). β- and γ-cytoplasmic actins display distinct distribution and functional diversity. J. Cell Sci. *122*, 2980–2988. https://doi.org/10.1242/jcs.041970.

15. Vedula, P., Kurosaka, S., Leu, N.A., Wolf, Y.I., Shabalina, S.A., Wang, J., Sterling, S., Dong, D.W., and Kashina, A. (2017). Diverse functions of homologous actin isoforms are defined by their nucleotide, rather than their amino acid sequence. eLife *6*, e31661. https://doi.org/10.7554/eLife.31661.

16. Boiero Sanders, M., Toret, C.P., Guillotin, A., Antkowiak, A., Vannier, T., Robinson, R.C., and Michelot, A. (2022). Specialization of actin isoforms derived from the loss of key interactions with regulatory factors. EMBO J. *41*, e107982. https://doi.org/10.15252/embj.2021107982.

17. Michelot, A., and Drubin, D.G. (2011). Building Distinct Actin Filament Networks Review in a Common Cytoplasm. Curr. Biol. *21*, R560–R569.

18. Serobyan, V., Kontarakis, Z., El-Brolosy, M.A., Welker, J.M., Tolstenkov, O., Saadeldein, A.M., Retzer, N., Gottschalk, A., Wehman, A.M., and Stainier, D.Y. (2020). Transcriptional adaptation in Caenorhabditis elegans. eLife *9*, e50014. https://doi.org/10.7554/eLife.50014.

19. Welker, J.M., Serobyan, V., Zaker Esfahani, E., and Stainier, D.Y.R. (2023). Partial sequence identity in a 25-nucleotide long element is sufficient for transcriptional adaptation in the Caenorhabditis elegans act-5/act-3 model. PLoS Genet. *19*, e1010806. https://doi.org/10.1371/journal.pgen.1010806.

20. Greve, J.N., Marquardt, A., Heiringhoff, R., Reindl, T., Thiel, C., Di Donato, N., Taft, M.H., and Manstein, D.J. (2024). The non-muscle actinopathy-associated mutation E334Q in cytoskeletal γ-actin perturbs interaction of actin filaments with myosin and ADF/cofilin family proteins. eLife *12*, RP93013. https://doi.org/10.7554/eLife.93013.

21. Greve, J.N., Schwäbe, F.V., Pokrant, T., Faix, J., Di Donato, N., Taft, M.H., and Manstein, D.J. (2022). Frameshift mutation S368fs in the gene encoding cytoskeletal β-actin leads to ACTB-associated syndromic thrombocytopenia by impairing actin dynamics. Eur. J. Cell Biol. *101*, 151216. https://doi.org/10.1016/j.ejcb.2022.151216.

22. Greve, J.N., and Manstein, D.J. (2025). Molecular mechanisms of hotspot variants in cytoskeletal β-actin associated with Baraitser-Winter syndrome. FEBS J. https://doi.org/10.1111/febs.70018.

23. Patrinostro, X., Roy, P., Lindsay, A., Chamberlain, C.M., Sundby, L.J., Starker, C.G., Voytas, D.F., Ervasti, J.M., and Perrin, B.J. (2018). Essential nucleotide- and protein-dependent functions of *Actb* /β-actin. Proc. Natl. Acad. Sci. *115*, 7973–7978. https://doi.org/10.1073/pnas.1807895115.

882 24. Bunnell, T.M., and Ervasti, J.M. (2010). Delayed embryonic development and impaired cell growth
883 and survival in *Actg1* null mice. Cytoskeleton *67*, 564–572. https://doi.org/10.1002/cm.20467.

884 25. Bunnell, T.M., Burbach, B.J., Shimizu, Y., and Ervasti, J.M. (2011). β-Actin specifically controls cell
885 growth, migration, and the G-actin pool. Mol. Biol. Cell *22*, 4047–4058.
886 https://doi.org/10.1091/mbc.e11-06-0582.

887 26. Vanslembrouck, B., Ampe, C., and Van Hengel, J. (2020). Time for rethinking the different β-actin
888 transgenic mouse models? Cytoskeleton *77*, 527–543. https://doi.org/10.1002/cm.21647.

889 27. Duan, Y., Li, L., Panzade, G.P., Piton, A., Zinovyeva, A., and Ambros, V. (2024). Modeling
890 neurodevelopmental disorder-associated human AGO1 mutations in Caenorhabditis elegans
891 Argonaute alg-1. Proc. Natl. Acad. Sci. U. S. A. *121*, e2308255121.
892 https://doi.org/10.1073/pnas.2308255121.

893 28. Hayashi, Y., Ono, K., and Ono, S. (2019). Mutations in Caenorhabditis elegans actin, which are
894 equivalent to human cardiomyopathy mutations, cause abnormal actin aggregation in nematode
895 striated muscle. F1000Research *8*, 279. https://doi.org/10.12688/f1000research.18476.1.

896 29. Willis, J.H., Munro, E., Lyczak, R., and Bowerman, B. (2006). Conditional Dominant Mutations in the
897 Caenorhabditis elegans Gene act-2 Identify Cytoplasmic and Muscle Roles for a Redundant Actin
898 Isoform. Mol. Biol. Cell *17*, 1051–1064. https://doi.org/10.1091/mbc.e05-09-0886.

899 30. Ono, S., and Pruyne, D. (2012). Biochemical and cell biological analysis of actin in the nematode
900 Caenorhabditis elegans. METHODS *56*, 11–17.

901 31. Ono, S. (2014). Regulation of Structure and Function of Sarcomeric Actin Filaments in Striated
902 Muscle of the Nematode *Caenorhabditis elegans*. Anat. Rec. *297*, 1548–1559.
903 https://doi.org/10.1002/ar.22965.

904 32. Krause, M., Wild, M., Rosenzweig, B., and Hirsh, D. (1989). Wild-type and mutant actin genes in
905 Caenorhabditis elegans. J. Mol. Biol. *208*, 381–392. https://doi.org/10.1016/0022-2836(89)90503-2.

906 33. Landel, C.P., Krause, M., Waterston, R.H., and Hirsh, D. (1984). DNA rearrangements of the actin
907 gene cluster in Caenorhabditis elegans accompany reversion of three muscle mutants. J. Mol. Biol.
908 *180*, 497–513. https://doi.org/10.1016/0022-2836(84)90024-x.

909 34. Avery, L. (1993). The genetics of feeding in Caenorhabditis elegans. Genetics *133*, 897–917.
910 https://doi.org/10.1093/genetics/133.4.897.

911 35. MacQueen, A.J., Baggett, J.J., Perumov, N., Bauer, R.A., Januszewski, T., Schriefer, L., and Waddle,
912 J.A. (2005). ACT-5 Is an Essential Caenorhabditis elegans Actin Required for Intestinal Microvilli
913 Formation. Mol. Biol. Cell *16*, 3247–3259. https://doi.org/10.1091/mbc.e04-12-1061.

914 36. Paix, A., Folkmann, A., Rasoloson, D., and Seydoux, G. (2015). High Efficiency, Homology-Directed
915 Genome Editing in Caenorhabditis elegans Using CRISPR-Cas9 Ribonucleoprotein Complexes.
916 Genetics *201*, 47–54.

917 37. Chacon-Camacho, O.F., Barragán-Arévalo, T., Villarroel, C.E., Almanza-Monterrubio, M., and
918 Zenteno, J.C. (2020). Previously undescribed phenotypic findings and novel *ACTG1* gene pathogenic
919 variants in Baraitser-Winter cerebrofrontofacial syndrome. Eur. J. Med. Genet. *63*, 103877.
920 https://doi.org/10.1016/j.ejmg.2020.103877.

921 38. Vontell, R., Supramaniam, V.G., Davidson, A., Thornton, C., Marnerides, A., Holder-Espinasse, M.,
922 Lillis, S., Yau, S., Jansson, M., Hagberg, H.E., et al. (2019). Post-mortem Characterisation of a Case
923 With an ACTG1 Variant, Agenesis of the Corpus Callosum and Neuronal Heterotopia. Front. Physiol.
924 *10*.

925 39. Cianci, P., Fazio, G., Casagranda, S., Spinelli, M., Rizzari, C., Cazzaniga, G., and Selicorni, A. (2017).
926 Acute myeloid leukemia in Baraitser–Winter cerebrofrontofacial syndrome. Am. J. Med. Genet. A.
927 *173*, 546–549. https://doi.org/10.1002/ajmg.a.38057.

928 40. Cai, E.D., Sun, B.K., Chiang, A., Rogers, A., Bernet, L., Cheng, B., Teng, J., Rieger, K.E., and Sarin, K.Y.
929 (2017). Postzygotic Mutations in Beta-Actin Are Associated with Becker's Nevus and Becker's Nevus
930 Syndrome. J. Invest. Dermatol. *137*, 1795–1798. https://doi.org/10.1016/j.jid.2017.03.017.

931 41. Happle, R. (2017). Becker's Nevus and Lethal Beta-Actin Mutations. J. Invest. Dermatol. *137*, 1619–
932 1621. https://doi.org/10.1016/j.jid.2017.04.003.

933 42. Eggink, H., van Egmond, M.E., Verschuuren-Bemelmans, C.C., Schönherr, M.C., de Koning, T.J.,
934 Oterdoom, D.L.M., van Dijk, J.M.C., and Tijssen, M.A.J. (2017). Dystonia-deafness syndrome caused
935 by a β-actin gene mutation and response to deep brain stimulation. Mov. Disord. *32*, 162–165.
936 https://doi.org/10.1002/mds.26842.

937 43. Conboy, E., Vairo, F., Waggoner, D., Ober, C., Das, S., Dhamija, R., Klee, E.W., and Pichurin, P. (2017).
938 Pathogenic Variant in ACTB, p.Arg183Trp, Causes Juvenile-Onset Dystonia, Hearing Loss, and
939 Developmental Delay without Midline Malformation. Case Rep. Genet. *2017*, 9184265.
940 https://doi.org/10.1155/2017/9184265.

941 44. Gearing, M., Juncos, J.L., Procaccio, V., Gutekunst, C.-A., Marino-Rodriguez, E.M., Gyure, K.A., Ono,
942 S., Santoianni, R., Krawiecki, N.S., Wallace, D.C., et al. (2002). Aggregation of actin and cofilin in
943 identical twins with juvenile-onset dystonia. Ann. Neurol. *52*, 465–476.
944 https://doi.org/10.1002/ana.10319.

945 45. Procaccio, V., Salazar, G., Ono, S., Styers, M.L., Gearing, M., Davila, A., Jimenez, R., Juncos, J.,
946 Gutekunst, C.-A., Meroni, G., et al. (2006). A mutation of beta -actin that alters depolymerization
947 dynamics is associated with autosomal dominant developmental malformations, deafness, and
948 dystonia. Am. J. Hum. Genet. *78*, 947–960. https://doi.org/10.1086/504271.

949 46. Zech, M., Jech, R., Wagner, M., Mantel, T., Boesch, S., Nocker, M., Jochim, A., Berutti, R.,
950 Havránková, P., Fečíková, A., et al. (2017). Molecular diversity of combined and complex dystonia:
951 insights from diagnostic exome sequencing. Neurogenetics *18*, 195–205.
952 https://doi.org/10.1007/s10048-017-0521-9.

953 47. Skogseid, I.M., Røsby, O., Konglund, A., Connelly, J.P., Nedregaard, B., Jablonski, G.E., Kvernmo, N.,
954 Stray-Pedersen, A., and Glover, J.C. (2018). Dystonia-deafness syndrome caused by ACTB

955 p.Arg183Trp heterozygosity shows striatal dopaminergic dysfunction and response to pallidal
956 stimulation. J. Neurodev. Disord. *10*, 17. https://doi.org/10.1186/s11689-018-9235-z.

957 48. Freitas, J.L., Vale, T.C., Barsottini, O.G.P., and Pedroso, J.L. (2019). Expanding the Phenotype of
958 Dystonia-Deafness Syndrome Caused by ACTB Gene Mutation. Mov. Disord. Clin. Pract. *7*, 86–87.
959 https://doi.org/10.1002/mdc3.12854.

960 49. Oosterheert, W., Blanc, F.E.C., Roy, A., Belyy, A., Sanders, M.B., Hofnagel, O., Hummer, G., Bieling,
961 P., and Raunser, S. (2023). Molecular mechanisms of inorganic-phosphate release from the core and
962 barbed end of actin filaments. Nat. Struct. Mol. Biol. *30*, 1774–1785.
963 https://doi.org/10.1038/s41594-023-01101-9.

964 50. Marquardt, A., Münchhoff, M.S., Krohn, J., Palarz, P.M., Taft, M.H., Greve, J.N., Di Donato, N.,
965 Buettner, F.F.R., and Manstein, D.J. (2025). Disruption of SETD3-mediated histidine-73 methylation
966 by the BWCFF-associated β-actin G74S mutation. FEBS Lett. https://doi.org/10.1002/1873-
967 3468.70088.

968 51. Dominguez, R., and Holmes, K.C. (2011). Actin Structure and Function. Annu. Rev. Biophys. *40*, 169–
969 186. https://doi.org/10.1146/annurev-biophys-042910-155359.

970 52. Rubenstein, P.A., and Wen, K. (2014). Insights into the effects of disease-causing mutations in
971 human actins. Cytoskeleton *71*, 211–229. https://doi.org/10.1002/cm.21169.

972 53. Reynolds, M.J., Hachicho, C., Carl, A.G., Gong, R., and Alushin, G.M. (2022). Bending forces and
973 nucleotide state jointly regulate F-actin structure. Nature *611*, 380–386.
974 https://doi.org/10.1038/s41586-022-05366-w.

975 54. Ferguson, E.L., and Horvitz, H.R. (1985). Identification and characterization of 22 genes that affect
976 the vulval cell lineages of the nematode Caenorhabditis elegans. Genetics *110*, 17–72.
977 https://doi.org/10.1093/genetics/110.1.17.

978 55. Ly, K., Reid, S.J., and Snell, R.G. (2015). Rapid RNA analysis of individual Caenorhabditis elegans.
979 MethodsX *2*, 59–63. https://doi.org/10.1016/j.mex.2015.02.002.

980 56. Schafer, W. (2005). Egg-laying. WormBook.

981 57. Bauer, J., Poupart, V., Goupil, E., Nguyen, K.C.Q., Hall, D.H., and Labbé, J.-C. (2021). The initial
982 expansion of the C. elegans syncytial germ line is coupled to incomplete primordial germ cell
983 cytokinesis. Dev. Camb. Engl. *148*, dev199633. https://doi.org/10.1242/dev.199633.

984 58. Green, R.A., Kao, H.-L., Audhya, A., Arur, S., Mayers, J.R., Fridolfsson, H.N., Schulman, M.,
985 Schloissnig, S., Niessen, S., Laband, K., et al. (2011). A high-resolution C. elegans essential gene
986 network based on phenotypic profiling of a complex tissue. Cell *145*, 470–482.
987 https://doi.org/10.1016/j.cell.2011.03.037.

988 59. Marston, D.J., and Goldstein, B. (2006). Actin-based forces driving embryonic morphogenesis in
989 Caenorhabditis elegans. Curr. Opin. Genet. Dev. *16*, 392–398.

990 60. Vuong-Brender, T.T.K., Yang, X., and Labouesse, M. (2016). C. elegans Embryonic Morphogenesis. In
991 Current Topics in Developmental Biology (Elsevier), pp. 597–616.
992 https://doi.org/10.1016/bs.ctdb.2015.11.012.

993 61. Nance, J. (2005). Gastrulation in C. elegans. WormBook.

994 62. Zhang, P., Medwig-Kinney, T.N., and Goldstein, B. (2023). Architecture of the cortical actomyosin
995 network driving apical constriction in *C. elegans*. J. Cell Biol. *222*, e202302102.
996 https://doi.org/10.1083/jcb.202302102.

997 63. Bernadskaya, Y.Y., Wallace, A., Nguyen, J., Mohler, W.A., and Soto, M.C. (2012). UNC-40/DCC, SAX-
998 3/Robo, and VAB-1/Eph Polarize F-Actin during Embryonic Morphogenesis by Regulating the
999 WAVE/SCAR Actin Nucleation Complex. PLoS Genet. *8*, e1002863.
1000 https://doi.org/10.1371/journal.pgen.1002863.s003.

1001 64. Vuong-Brender, T.T.K., Ben Amar, M., Pontabry, J., and Labouesse, M. (2017). The interplay of
1002 stiffness and force anisotropies drives embryo elongation. eLife *6*, e23866.
1003 https://doi.org/10.7554/eLife.23866.

1004 65. Ennomani, H., Letort, G., Guérin, C., Martiel, J.-L., Cao, W., Nédélec, F., De La Cruz, E.M., Théry, M.,
1005 and Blanchoin, L. (2016). Architecture and Connectivity Govern Actin Network Contractility. Curr.
1006 Biol., 1–12.

1007 66. Reymann, A.-C., Staniscia, F., Erzberger, A., Salbreux, G., and Grill, S.W. (2016). Cortical flow aligns
1008 actin filaments to form a furrow. eLife *5*, e17807.

1009 67. Rose, L., and Gönczy, P. (2014). Polarity establishment, asymmetric division and segregation of fate
1010 determinants in early C. elegans embryos. WormBook, 1–43.

1011 68. Delattre, M., and Goehring, N.W. (2021). The first steps in the life of a worm: Themes and variations
1012 in asymmetric division in C. elegans and other nematodes. Curr. Top. Dev. Biol. *144*, 269–308.
1013 https://doi.org/10.1016/bs.ctdb.2020.12.006.

1014 69. Dorn, J.F., Zhang, L., Paradis, V., Edoh-Bedi, D., Jusu, S., Maddox, P.S., and Maddox, A.S. (2010).
1015 Actomyosin Tube Formation in Polar Body Cytokinesis Requires Anillin in C. elegans. Curr. Biol. *20*,
1016 2046–2051.

1017 70. Flynn, J.R., and McNally, F.J. (2017). A casein kinase 1 prevents expulsion of the oocyte meiotic
1018 spindle into a polar body by regulating cortical contractility. Mol. Biol. Cell *28*, 2410–2419.
1019 https://doi.org/10.1091/mbc.e17-01-0056.

1020 71. Charras, G., and Paluch, E. (2008). Blebs lead the way: how to migrate without lamellipodia. Nat.
1021 Rev. Mol. Cell Biol. *9*, 730–736. https://doi.org/10.1038/nrm2453.

1022 72. Pacquelet, A., Jousseaume, M., Etienne, J., and Michaux, G. (2019). Simultaneous Regulation of
1023 Cytokinetic Furrow and Nucleus Positions by Cortical Tension Contributes to Proper DNA
1024 Segregation during Late Mitosis. Curr. Biol. *29*, 3766-3777.e4.
1025 https://doi.org/10.1016/j.cub.2019.09.013.

1026 73. Lesanpezeshki, L., Hewitt, J.E., Laranjeiro, R., Antebi, A., Driscoll, M., Szewczyk, N.J., Blawzdziewicz,
1027 J., Lacerda, C.M.R., and Vanapalli, S.A. (2019). Pluronic gel-based burrowing assay for rapid
1028 assessment of neuromuscular health in C. elegans. Sci. Rep. *9*, 15246.
1029 https://doi.org/10.1038/s41598-019-51608-9.

1030 74. Yemini, E., Lin, A., Nejatbakhsh, A., Varol, E., Sun, R., Mena, G.E., Samuel, A.D.T., Paninski, L.,
1031 Venkatachalam, V., and Hobert, O. (2021). NeuroPAL: A Multicolor Atlas for Whole-Brain Neuronal
1032 Identification in C. elegans. Cell *184*, 272-288.e11. https://doi.org/10.1016/j.cell.2020.12.012.

1033 75. Tondeleir, D., Lambrechts, A., Müller, M., Jonckheere, V., Doll, T., Vandamme, D., Bakkali, K.,
1034 Waterschoot, D., Lemaistre, M., Debeir, O., et al. (2012). Cells Lacking β-Actin are Genetically
1035 Reprogrammed and Maintain Conditional Migratory Capacity*. Mol. Cell. Proteomics *11*, 255–271.
1036 https://doi.org/10.1074/mcp.M111.015099.

1037 76. Skruber, K., Read, T.-A., and Vitriol, E.A. (2018). Reconsidering an active role for G-actin in
1038 cytoskeletal regulation. J. Cell Sci. *131*, jcs203760-11.

1039 77. Rodriguez, A., and Kashina, A. (2018). Posttranscriptional and posttranslational regulation of actin.
1040 Anat. Rec. Hoboken NJ 2007 *301*, 1991–1998. https://doi.org/10.1002/ar.23958.

1041 78. Wilkinson, A.W., Diep, J., Dai, S., Liu, S., Ooi, Y.S., Song, D., Li, T.-M., Horton, J.R., Zhang, X., Liu, C., et
1042 al. (2019). SETD3 is an actin histidine methyltransferase that prevents primary dystocia. Nature *565*,
1043 372–376. https://doi.org/10.1038/s41586-018-0821-8.

1044 79. Ono, K. (2003). Specific requirement for two ADF/cofilin isoforms in distinct actin-dependent
1045 processes in Caenorhabditis elegans. J. Cell Sci. *116*, 2073–2085.

1046 80. Hall, D.H., Herndon, L.A., and Altun, Z. (2017). Introduction to C. elegans Embryo Anatomy.
1047 WormAtlas. https://doi.org/doi:10.3908/wormatlas.4.1.

1048 81. Xiao, L., Fan, D., Qi, H., Cong, Y., and Du, Z. (2022). Defect-buffering cellular plasticity increases
1049 robustness of metazoan embryogenesis. Cell Syst. *13*, 615-630.e9.
1050 https://doi.org/10.1016/j.cels.2022.07.001.

1051 82. Wang, S., Ochoa, S.D., Khaliullin, R.N., Gerson-Gurwitz, A., Hendel, J.M., Zhao, Z., Biggs, R., Chisholm,
1052 A.D., Desai, A., Oegema, K., et al. (2019). A high-content imaging approach to profile *C. elegans*
1053 embryonic development. Development *146*, dev174029. https://doi.org/10.1242/dev.174029.

1054 83. Green, R.A., Khaliullin, R.N., Zhao, Z., Ochoa, S.D., Hendel, J.M., Chow, T.-L., Moon, H., Biggs, R.J.,
1055 Desai, A., and Oegema, K. (2024). Automated profiling of gene function during embryonic
1056 development. Cell *187*, 3141-3160.e23. https://doi.org/10.1016/j.cell.2024.04.012.

1057 84. Waliman, M., Johnson, R.L., Natesan, G., Peinado, N.A., Tan, S., Santella, A., Hong, R.L., and Shah,
1058 P.K. (2024). Automated cell lineage reconstruction using label-free 4D microscopy. Genetics *228*,
1059 iyae135. https://doi.org/10.1093/genetics/iyae135.

1060 85. Naganathan, S.R., Fürthauer, S., Rodriguez, J., Fievet, B.T., Jülicher, F., Ahringer, J., Cannistraci, C.V.,
1061 and Grill, S.W. (2018). Morphogenetic degeneracies in the actomyosin cortex. eLife *7*, e37677.
1062 https://doi.org/10.7554/eLife.37677.

1063 86. Priess, J.R., and Hirsh, D.I. (1986). Caenorhabditis elegans morphogenesis: the role of the
1064 cytoskeleton in elongation of the embryo. Dev. Biol. *117*, 156–173. https://doi.org/10.1016/0012-
1065 1606(86)90358-1.

1066 87. Quintin, S., Wang, S., Pontabry, J., Bender, A., Robin, F., Hyenne, V., Landmann, F., Gally, C.,
1067 Oegema, K., and Labouesse, M. (2018). Correction: Non-centrosomal epidermal microtubules act in
1068 parallel to LET-502/ROCK to promote *C. elegans* elongation (doi:10.1242/dev.126615). Development
1069 *145*, dev167262. https://doi.org/10.1242/dev.167262.

1070 88. Riva, C., Hajduskova, M., Gally, C., Suman, S.K., Ahier, A., and Jarriault, S. (2022). A natural
1071 transdifferentiation event involving mitosis is empowered by integrating signaling inputs with
1072 conserved plasticity factors. Cell Rep. *40*, 111365. https://doi.org/10.1016/j.celrep.2022.111365.

1073 89. Chai, Y., Tian, D., Zhu, Z., Jiang, Y., Huang, S., Wu, D., Ou, G., and Li, W. (2022). Wnt signaling
1074 polarizes cortical actin polymerization to increase daughter cell asymmetry. Cell Discov. *8*, 22.
1075 https://doi.org/10.1038/s41421-022-00376-4.

1076 90. Budirahardja, Y., and Gönczy, P. (2008). PLK-1 asymmetry contributes to asynchronous cell division
1077 of *C. elegans* embryos. Development *135*, 1303–1313. https://doi.org/10.1242/dev.019075.

1078 91. The C. elegans Deletion Mutant Consortium (2012). Large-Scale Screening for Targeted Knockouts in
1079 the *Caenorhabditis elegans* Genome. G3 GenesGenomesGenetics *2*, 1415–1425.
1080 https://doi.org/10.1534/g3.112.003830.

1081 92. Brenner, S. (1974). THE GENETICS OF CAENORHABDITIS ELEGANS. Genetics *77*, 71.

1082 93. Pasturel, A., Strale, P.-O., and Studer, V. (2020). Tailoring Common Hydrogels into 3D Cell Culture
1083 Templates. Adv. Healthc. Mater. *9*, 2000519. https://doi.org/10.1002/adhm.202000519.

1084 94. Yemini, E., Jucikas, T., Grundy, L.J., Brown, A.E.X., and Schafer, W.R. (2013). A database of C. elegans
1085 behavioral phenotypes. Nat. Methods *10*, 877–879. https://doi.org/10.1038/nmeth.2560.

1086 95. Hoogewijs, D., Houthoofd, K., Matthijssens, F., Vandesompele, J., and Vanfleteren, J.R. (2008).
1087 Selection and validation of a set of reliable reference genes for quantitative sod gene expression
1088 analysis in C. elegans. BMC Mol. Biol. *9*, 9. https://doi.org/10.1186/1471-2199-9-9.

1089 96. Jumper, J., Evans, R., Pritzel, A., Green, T., Figurnov, M., Ronneberger, O., Tunyasuvunakool, K.,
1090 Bates, R., Žídek, A., Potapenko, A., et al. (2021). Highly accurate protein structure prediction with
1091 AlphaFold. Nature *596*, 583–589. https://doi.org/10.1038/s41586-021-03819-2.

1092 97. Schutt, C.E., Myslik, J.C., Rozycki, M.D., Goonesekere, N.C.W., and Lindberg, U. (1993). The structure
1093 of crystalline profilin–β-actin. Nature *365*, 810–816. https://doi.org/10.1038/365810a0.

1094 98. Waterhouse, A., Bertoni, M., Bienert, S., Studer, G., Tauriello, G., Gumienny, R., Heer, F.T., de Beer,
1095 T.A.P., Rempfer, C., Bordoli, L., et al. (2018). SWISS-MODEL: homology modelling of protein
1096 structures and complexes. Nucleic Acids Res. *46*, W296–W303. https://doi.org/10.1093/nar/gky427.

1097 99. Arora, A.S., Huang, H.-L., Singh, R., Narui, Y., Suchenko, A., Hatano, T., Heissler, S.M.,
1098 Balasubramanian, M.K., and Chinthalapudi, K. (2023). Structural insights into actin isoforms. eLife
1099 *12*, e82015. https://doi.org/10.7554/eLife.82015.

1100 100. Pettersen, E.F., Goddard, T.D., Huang, C.C., Meng, E.C., Couch, G.S., Croll, T.I., Morris, J.H., and
1101 Ferrin, T.E. (2021). UCSF ChimeraX: Structure visualization for researchers, educators, and
1102 developers. Protein Sci. Publ. Protein Soc. *30*, 70–82. https://doi.org/10.1002/pro.3943.

1103

1104 **STAR★METHODS**

1105 **KEY RESOURCES TABLE**

REAGENT or RESOURCE	SOURCE	IDENTIFIER
Restriction enzyme: BfuI	Thermo Fisher Scientific	ER1501
Restriction enzyme: BsmF1	New England Biolabs	R0572L
Restriction enzyme: PciI	New England Biolabs	R0655L
Restriction enzyme: BsaBI	Thermo Fisher Scientific	ER1711
Restriction enzyme: AccI	New England Biolabs	R0161L
Restriction enzyme: HaeIII	New England Biolabs	R018L
Restriction enzyme: BglII	New England Biolabs	R0144L
Restriction enzyme: AlwI	New England Biolabs	R0513S
Restriction enzyme: MspA1I	New England Biolabs	R0577S
Cas9	homemade	
F-127	Sigma-Aldrich	P2443 ; CAS: 9003-11-6
5 mM Tris-HCl pH 8.0	Euromedex	EU0011
Triton X-100	Sigma-Aldrich	93418
Tween 20	Sigma-Aldrich	P2287
EDTA	Euromedex	EU0007
1 mg/mL proteinase K	Thermo Fisher Scientific	EO0491
Levamisole	Eurobio Scientific	SP-5000-18
Sodium Azide	Interchimsa	NJK63A
Critical commercial assays		
Maxima H Minus First Strand cDNA Synthesis Kit	Thermo Fisher Scientific	K1651
Lightcycler® 480 SYBR Green | Master mix	Roche Life Science	04887352001

Experimental models: Organisms/strains		
C. elegans: Strain ACR061: act-2(rey012 [Leu65Val]) V	This paper	N/A
C. elegans: Strain ACR096: nmy-2(cp7[nmy-2::gfp + LoxP unc-119(+) LoxP]) I; gesIs001([mex-5p::Lifeact::mKate::nmy-2UTR, unc-119(+)]) ; act-2 (rey012[Leu65Val]) V	This paper	N/A
C. elegans: Strain ACR153: otIs696 ; act-2(rey012 [Leu65Val]) V	This paper	N/A
C. elegans: Strain ACR108: act-2(rey022 [Gly74Ser]) V	This paper	N/A
C. elegans: Strain ACR224: nmy-2(cp7[nmy-2::gfp + LoxP unc-119(+) LoxP]) I; gesIs001([mex-5p::Lifeact::mKate::nmy-2UTR, unc-119(+)]) ; act-2 (rey022[Gly74Ser]) V	This paper	N/A
C. elegans: Strain ACR165: otIs696 ; act-2(rey022 [Gly74Ser]) V	This paper	N/A
C. elegans: Strain ACR070: act-2(rey014 [Thr120Ile]) V	This paper	N/A
C. elegans: Strain ACR139: nmy-2(cp7[nmy-2::gfp + LoxP unc-119(+) LoxP]) I; gesIs001([mex-5p::Lifeact::mKate::nmy-2UTR, unc-119(+)]) ; act-2 (rey014[Thr120Ile]) V	This paper	N/A
C. elegans: Strain ACR137: otIs696 ; act-2(rey014 [Thr120Ile]) V	This paper	N/A
C. elegans: Strain ACR168: act-2(syb3920 [Arg147Ser]/nT1[qIs50])	This paper	N/A
C. elegans: Strain ACR216: otIs696 ; act-2(syb3920[Arg147Ser]/nT1[qIs51]) V	This paper	N/A
C. elegans: Strain PHX5567: act-2(syb5567 [Arg183Thr]) V	This paper	N/A
C. elegans: Strain ACR125: act-2 (syb3909[Arg196Cys]) V	This paper	N/A
C. elegans: Strain ACR135: nmy-2(cp7[nmy-2::gfp + LoxP unc-119(+) LoxP]) I; gesIs001 ([mex-5p::Lifeact::mKate::nmy-2UTR, unc-119(+)]) ; act-2 (syb3909[Arg196Cys]) V	This paper	N/A
C. elegans: Strain ACR166: otIs696 ; act-2 (syb3909[Arg196Cys]) V	This paper	N/A
C. elegans: Strain ACR085: act-2(rey020 [Arg196His]) V	This paper	N/A
C. elegans: Strain ACR107: nmy-2(cp7[nmy-2::gfp + LoxP unc-119(+) LoxP]) I; gesIs001([mex-5p::Lifeact::mKate::nmy-2UTR, unc-119(+)]) ; act-2 (rey020[Arg196His]) V	This paper	N/A
C. elegans: Strain ACR136: otIs696 ; act-2(rey020[Arg196His]) V	This paper	N/A
C. elegans: Strain ACR099: act-2 (rey023[Thr203Met])/nT1[qIs50] (IV;V)	This paper	N/A

C. elegans: Strain ACR122: gesIs001([mex-5p::Lifeact::mKate::nmy-2UTR, unc-119(+)]) ; act-2 (rey023[Thr203Met])/nT1[qIs50] (IV;V)	This paper	N/A
C. elegans: Strain ACR219: otIs696 ; act-2(rey023[Thr203Met]) / nT1[qIs50] (IV;V)	This paper	N/A
C. elegans: Strain EU1383: act-2(ok1229) V	Willis *et al*.,[29]	WB Strain: EU1383; WormBase: WBStrain00007359
C. elegans: Strain ACR162: act-2(ok1229) V	This paper	N/A
C. elegans: Strain ACR161: act-2(rey016) V	This paper	N/A
C. elegans: Strain ACR149: act-2(rey021) V	This paper	N/A
C. elegans: Strain ACR173: otIs696 ; act-2(rey021) V	This paper	N/A
C. elegans: Strain DW101: atl-1(tm853) V/ nT1[qIs50] (IV;V)	Budurahardja and Gönczy[90]	WB Strain: DW101; WormBase: WBStrain00006438
C. elegans: Strain VC854: unc-2(gk366) X	The *C. elegans* Deletion Mutant Consortium[91]	WB Strain: VC854; WormBase: WBStrain00036122
C. elegans: Strain SWG007: nmy-2(cp7[nmy-2::gfp + LoxP unc-119(+) LoxP]) I; gesIs001([mex-5p::Lifeact::mKate2::nmy-2UTR, unc-119(+)])	Reymann et al.[66]	
C. elegans: Strain OH15495: otIs696	Yemini et al.[74]	WB Strain: OH15495; WormBase: WBStrain00047403
C. elegans: Strain N2	Brenner[92]	WB Strain: N2; WormBase: WBStrain00000001
Oligonucleotides		
Primers for genotyping	See Table S1	N/A
Primers for RT-qPCR	See Table S1	N/A
Recombinant DNA		
CRISPR guides and repair templates	See Table S2	IDT
Software and algorithms		

ImageJ		https://imagej.nih.gov/ij/
NeuroPAL	Yemini et al.[74]	NeuroPAL — Yemini Lab
SnapGene		
R 4.4.1	The R Project for Statistical Computing	Index of /bin/windows/base/old/4.4.1
R-Studio 2023.12.1	RStudio Integrated Development Environment	2023.12.1+402.pro1
JAGS 4.3.2.	Just Another Gibbs Sampler	JAGS - Just Another Gibbs Sampler
Other		
Idylle® 9 well Stencell	Pasturel et al.[93]	

1106
1107
1108 **METHOD DETAILS**

1109 ***C. elegans* handling**

1110 Animals were cultured at 20°C on Nematode Growth Medium plates seeded with OP50[92].
1111 Bristol strain (N2) was used as a reference. We thank the Caenorhabditis Genetics Center for
1112 providing the strains N2, DW101 and EU1383. All novel actin variants models were generated in
1113 the Reymann lab except for two alleles *act-2(syb3920)* and *act-2(syb5567)*, which were
1114 outsourced to Suny Biotech®.

1115 ***C. elegans* generation**

1116 Importantly, note that *C. elegans* actins including ACT-2 possesses an additional Cysteine
1117 after the initial Methionine in the N-terminus compared to Human ACTB and ACTG1 (ACTB being
1118 MDDDIAA and ACT-2 MCDDDVAA, Figure S1A). For simplicity and easier correspondence to
1119 patient's variations, we however referred to *act-2 C. elegans* edited variants using the human
1120 amino acid (-1) numbering. For example, human variation ACTB p.L65V is referred to in this
1121 publication as *act-2* p.L65V instead of *act-2* L66V in the *C. elegans* frame.

1122 We performed *dpy-10* co-CRISPR editing using purified homemade Cas9 protein, synthetic
1123 tracrRNA, and ssODN, as described in Paix et al. 2015[36]. The table of crRNA and repair template
1124 used are listed in Supplementary Table 2. Additional silent mutations were introduced either to
1125 add or remove a restriction enzyme recognition site for genotyping strategies as well as to mutate
1126 PAM or nucleotides within the sgRNA. All generated strains were then outcrossed four times with
1127 the N2 strain and all actin coding genes were sequenced to verify that only *act-2* was mutated

1128 (genotyping primers available in Supplementary Table 1). Sequencing was performed by
1129 Eurofins® and analysed using SnapGene®.

1130 The *act-2(rey016)* allele consists of an insertion-deletion in exon 2 (33bp insertion + 816bp
1131 deletion) resulting in a frameshift and a premature STOP codon at the amino acid 70. The *act-*
1132 *2(rey021)* allele presents a 35bp insertion causing a frameshift and a premature STOP codon at
1133 the amino acid 120. The *act-2(ok1229)* presents a large deletion starting at the 213th amino acid
1134 and extending beyond the 3' UTR.

1135 **Egg-laying assay**

1136 The number of eggs laid by single hermaphrodite animals was quantified on 6-well plates by
1137 isolating and transferring individual animals from well to well every 24 hours. Animals were
1138 isolated at the L4 stage. After each transfer, eggs laid were manually counted. The number of
1139 larvae was manually counted to determine the hatching percentage 36-48 hours after the transfer.
1140 This process was repeated over the three days of the time course, otherwise indicated.

1141 Plates were blinded by someone external to the analysis and maintained at the desired
1142 temperature (15°C, 20°C, or 25°C) throughout the experiment. Whenever we observed
1143 contamination or premature death of the P0 animal, we excluded its dataset from the analysis.
1144 Each experiment was performed on around 15 animals including a WT control group on the same
1145 medium pour.

1146 Regarding figure 2D and S3A/C, we generated heterozygote animals by crossing L4-staged
1147 homozygous actin variants animals with N2 males and quantified the brood size of F1 animals
1148 (2E and S3B/D). After experiment completion, we verified each animal's genotype by sequencing
1149 their progeny (genotyping primers are available in Supplementary Table 1). In figure S3C/D
1150 heterozygous animals were obtained after a cross between N2 males and p.R147S/nT1 and
1151 p.T203M/nT1 heterozygous animals; but only non-nT1 (ie non-GFP fluorescent pharynx) animals
1152 were considered —hence the R147S/+ and T203M/+ maternal genotype.

1153 **3D motility assay**

1154 The ability of animals to move in a 3D medium was assessed using a pluronic-based
1155 burrowing assay as described in Lesanpezeshki et al [73] and optimized by Ana Carvahlo (personal
1156 communication) as follows. Liquid pluronic gel was made by adding 13g of F-127 powder into
1157 37mL of Ultra Pure water and leaving the solution at 4°C for 48 hours. At least an hour before the
1158 experiment, pluronic gel and consumables were put at 10°C and kept refrigerated unless

1159 otherwise stated. Animals were isolated at the L4 stage 24 hours before the experiment and
1160 blinded by someone external to the experiment. Each experiment included a WT control group.

1161 For each experiment, we put a 25µL drop of liquid pluronic gel in each well of a 24-well
1162 plate and added 10 animals into each drop. We left the plate at 20°C for a few minutes for the
1163 drop to set. Next, we added 1.3mL of liquid pluronic gel to each well to obtain a gel height of
1164 0.6µm. After waiting 10 minutes for the gel to solidify, we added a 10µL drop of fresh concentrated
1165 (100mg/mL) OP50 to use as a chemo-attractant and kept the plate at 20°C. Then, the number of
1166 animals that reached the well's top was manually counted every 10 minutes for two hours.

1167 The negative control, *unc-2(gk366)* is a knockout of the Human CACNA1B (calcium
1168 voltage-gated channel subunit alpha1 B) ortholog, thus predicted to enable high voltage-gated
1169 calcium channel activity expressed in whole body wall muscle and required for proper animal
1170 motility[94].

1171 **Chemo-sensation assay**

1172 To ensure that the 3D motility defects observed were unrelated to the animals' potential
1173 inability to sense food, we performed a standard chemosensation assay. Animals, isolated at the
1174 L4 stage 24 hours before the experiment were blinded by someone external to the experiment.
1175 Animals were washed 4 times in M9 and placed at the center of a 6cm plate NGM plate without
1176 food. Fresh concentrated (100mg/mL) OP50 and Ultra Pure H_2O were placed on opposite
1177 extremities of the plate. After one hour, the number of animals on each side of the plates was
1178 counted as well as the animals that did not move from their original positions ("Immobile animals"
1179 in Figure S5). The chemotaxis index was calculated using $I = \frac{n_{OP50} - n_{H_2O}}{n_{Total} - n_{immobile\ animals}}$.

1180 **RT-qPCR**

1181 Single animal RT-qPCR was performed as in Ly, Reid and Snell [55]. An hour before the
1182 experiment, we isolated L4 animals on a plate without food. Single L4 animals were transferred
1183 in 0.2mL Eppendorf tubes containing 2µL of lysis buffer (5 mM Tris-HCl pH 8.0, 0.5% Triton X-
1184 100, 0.5%, Tween 20, 0.25 mM EDTA and 1 mg/mL proteinase K) without sticking them with
1185 bacteria. Tubes were incubated at 65°C for 10 min, then at 85°C for 1min in a T100TM Thermal
1186 Cycler. After lysis completion, we used the Maxima H Minus cDNA synthesis kit. Genomic DNA
1187 was removed by adding 1µL of a master mix containing 1µL of dsDNAse buffer, 1µL of DsDNAse,
1188 and 8µL of nuclease-free water. The solution was incubated at 37°C for 2 minutes and
1189 immediately chilled on ice. cDNA synthesis was generated by adding 1µL of a mix containing

1190 0.5µL oligo dT primer, 0.5µL 10mM dNTP, 6.5µL nuclease-free water, 2µL RT buffer, and 0.5µL
1191 Maxima H Minus enzyme mix to the lysate. Tubes were centrifugated and incubated them at 25°C
1192 for 10 minutes, then at 55°C for 30 minutes, and finally 5 minutes at 85°C. We diluted the cDNA
1193 to 25 µL with nuclease-free water and used it immediately. We prepared 6 mixes of primer (*act-*
1194 *1, act-2, act-3, act-4, act-5,* and *iscu-1*) containing 30.6µL of PCR grade water, 7.2µL of the
1195 forward primer at 10µM, 7.2µL of the reverse primer at 10µM (Available in Supplementary Table
1196 1) and 90µL of the Lightcycler® 480 SYBR Green | Master mix. We added 7.5µL of primer mix
1197 for 2.5µL of lysis into a 384-well plate. We sealed the plate using the provided foil with gloves and
1198 centrifuged it at 1500xg for 2 minutes. We used a LightCycler® for qPCR following these steps;
1199 firstly a pre-incubation at 95°C for 15 minutes with a 4.4 ramp, secondly a step of amplification of
1200 45 cycles composed of 10 seconds at 95°C with a 4.4 ramp, 15 seconds at 54°C with a 2.2 ramp
1201 and 10 seconds at 72°C with a 4.4 ramp. Thirdly, a melting curve analysis composed of 5 seconds
1202 at 95°C with a 4.4 ramp, 65 seconds at 70°C with a 2.2 ramp, and continuous heating to reach
1203 95°C before cooling back at 40°C.

1204 The Cts measured by the Lightcycler® were exported to a text file and were analysed
1205 using R and Rstudio (see Key resources table). Values were normalised using the Ct values of
1206 the reference gene *iscu-1* [55,95] and to the N2 results of the same experiment. Some animals were
1207 excluded from analysis when their Ct values reached 40. Primer pairs efficiencies were measured
1208 using standard curve analysis available in Figure S2.

1209 **Microscopy**

1210 **Embryonic development time-lapse imaging**

1211 L4 animals were put on a plate at 20°C 24h before acquisition. To obtain embryos,
1212 dissections were performed on a slide covered with an Idylle® 9 well Stencell[93] with 5µL of M9
1213 and 4 animals of the desired genotype in each well. Then, corpses were removed from each well
1214 using a mouth micropipette. The slide containing the dissected animals was then stuck to a #1.5
1215 coverslip (Marienfeld Superior) and placed on a Zeiss Axio-Observer 7. DIC images were then
1216 acquired using a Hamamatsu orca flash 4.0 LT camera, every 10 seconds for 40 minutes and
1217 then every 10 minutes for at least 14 hours with a 20x/0.8 PLAN-Apochromat objective. Given the
1218 low frequency of some of the observed phenotypes, we deliberately chose to favour high
1219 throughput with low magnification at the expense of image quality: 9 wells were simultaneously
1220 acquired, thereby allowing replicates of 3 mutant conditions and 3 WT controls, representing in

1221 total ~20 to 25 (x,y) positions containing each 2 to 15 embryos simultaneously observed during
1222 overnight acquisitions. The room temperature was controlled and set to 20-22 degrees.

1223 **Early embryogenesis**

1224 L4 animals were put on a plate at 20°C 24 hours before acquisition. Dissection of 5 animals
1225 was performed in 5µL of M9. The slide containing the dissected animals was then placed on a
1226 2% agarose pad and placed on an inverted microscope Nikon EclipseTi-2 equipped with
1227 YOKOGAWA CSU X1 spinning disk head. Pictures were then acquired using a Photometrics
1228 Prime 95B camera each 2 or 10 second for 15 minutes with a plan apo 100x/1.45 Nikon objective.

1229 **Gonad imaging**

1230 L4 animals were immobilised in 10 µL of 1mM Levamisole and placed on a 2% agarose
1231 pad. Acquisition of gonads was performed on a LEICA DMI8 inverted microscope equipped with
1232 Yokogawa CSU W1 Spinning disk. Z-stacks were acquired using a Hamamatsu Orca Flash 4.0
1233 camera with a 40X HCX PL APO oil immersion objective with a 0.2µm Z-step. Gonad widths were
1234 measured using FIJI by drawing a line with a 120-pixel width across the gonads germs cells and
1235 rachis in front of the +1 oocyte. Classification of phenotypes was performed visually as
1236 represented in [58]. Heatmap was built using the heatmap.2 function from the R package gplots.
1237 The mean number of observed phenotypes for each variable was scaled in the row direction.

1238 **NeuroPal**

1239 L4 animals were immobilised in 7µL of 125mM sodium azide and placed on a 2% agarose
1240 pad. Acquisitions were made accordingly to https://www.hobertlab.org/wp-
1241 content/uploads/2019/09/Configuring-Your-Microscope-for-NeuroPAL-v2.pdf on a Confocal
1242 Inverted Leica TCS SP8X equipped with DMI6000 microscope White Light Laser using a 40x/1.3
1243 HC PL APO CS oil immersion objective with a distance of 0.9µm between each Z. Mapping and
1244 comparison of the expected expression pattern is performed using the NeuroPAL software and
1245 reference atlas map.

1246 **Principal Component Analysis**

1247 Principal Component Analysis (PCA) was computed and plotted using the FactoMineR
1248 package with the PCA function using 9 dimensions, we set the 'graph' argument to true to obtain
1249 the variables factor map presented in Figure S6A. Missing values were replaced by the mean of
1250 the corresponding variable. Matrices show the quality of representation of variables across
1251 dimensions and were constructed using the get_pca_var function from the FactoMineR package.

1252 We exported the coordinates of each point and calculated the distance between each point and
1253 the WT in the two first dimensions.

1254 ***In silico* analysis**

1255 The primary sequence of ACT-2 from *C. elegans* was obtained from the UniProt database
1256 (ID: P10984). We used Alphafold2 [96] to predict the structure of ACT-2 G-actin. Calculations were
1257 performed on the Halime HPC cluster at the Institute for Biophysical Chemistry at Hannover
1258 Medical School. We visualized ATP in the nucleotide binding cleft of ACT-2 G-actin by aligning
1259 the predicted ACT-2 structure with the structure of bovine ATP-bound G-actin (PDB-ID: 2BTF, [97]).
1260 The homology model of the ACT-2 filament was generated using the SWISS-MODEL server [98]
1261 with the ADP-bound human cytoskeletal β-actin filament (PDB-ID: 8DNH, [99] as a template.
1262 ChimeraX [100] was used for visualization of the structures and assessment of the potential
1263 implications of the variants for actin structure.

1264

1265 **QUANTIFICATION AND STATISTICAL ANALYSIS**

1266 We used R 4.4.1 through R-Studio 2023.12.1 and JAGS for all data analysis with all the
1267 required additional packages in their latest version available. All original code has been deposited
1268 and is publicly available via our Gitlab (https://gitlab.com/igbmc/reymannlab/2025-hecquet-
1269 iscience). The statistical analyses were performed in the frame of Bayesian and frequentist
1270 methods.

1271 **Bayesian Framework**

1272 The experimental data was enriched within the Bayesian framework by inference based
1273 on posterior distribution description. For embryonic lethality: Poisson distribution was used to
1274 estimate the embryonic lethality rates using an offset to account for the dependency with the
1275 number of eggs laid per animal (brood size) and specific parameters values for each genotype.
1276 Parameters were either given informative Normal priors: considering a very small lethality rate for
1277 WT N(0.01, 0.1), more probable lethality for all mutants N(0.1, 0.1) except the KO homozygotes
1278 for which we estimated a possible lethality of half the embryos N(0.5, 0.1). The analysis was also
1279 computed using low informative priors for all genotypes N(0,0.01) and gave similar results within
1280 a thousandth. Note that the observed 100% embryonic lethal genotypes were not included in the
1281 model. The posterior distribution was computed using the Markov chain Monte Carlo method
1282 (McMC). A burn-in of 2000 iterations, followed by 50000 iterations was used for each of the 3
1283 McMC chains, yielding a final 28800 iterations-sample for retrieving posterior distribution

1284 characteristics. Convergence of the McMC sample chains was checked graphically. Convergence
1285 was observed in each case. For each analysis on the main outcome, we computed the 95%
1286 credible interval of the embryonic failure rates for each genotype.

1287 Concerning the 3D motility assay, we compared the observed success rate to reach the
1288 chemoattractant after 2h by calculating their respective posterior distributions using two binomial
1289 distributions. We used the following priors: for WT mean = 0.9, sd=0.1 thus a probability modelled
1290 as p~dbeta(7.2, 0.8) and for all mutants a mean=0.5, sd=0.2 thus a probability modelled as
1291 p~dbeta(2.65, 2.65). A burn-in of 5000 iterations, followed by 105000 iterations was used for the
1292 McMC chain, in order to retrieve the posterior distributions. The odds ratio (OR), an estimation of
1293 the multiplication of the risk to fail reaching the target compared to WT, as well as the probability
1294 (p) that the difference between the two mean posterior probabilities is superior to 0.2 are indicated.

1295 **Frequentist Analysis**

1296 We used the R package rstatix for all frequentist statistical analyses. For multiple mean
1297 comparisons, we first verified the equality of variances and normality distribution of groups using
1298 a Levene and Shapiro test respectively. If those were verified, we realized an ANOVA test
1299 followed by a Tukey's range test. Otherwise, we realized a Kruskall-Wallis followed by a Dunn
1300 test. P-values obtained with the Dunn test were adjusted using the Bonferroni method.

1301 Statistics of Figure 5A were done on the values at the 2-hour timepoint. A summary of all
1302 tests and p-values is available in Supplementary Table 3.

1303

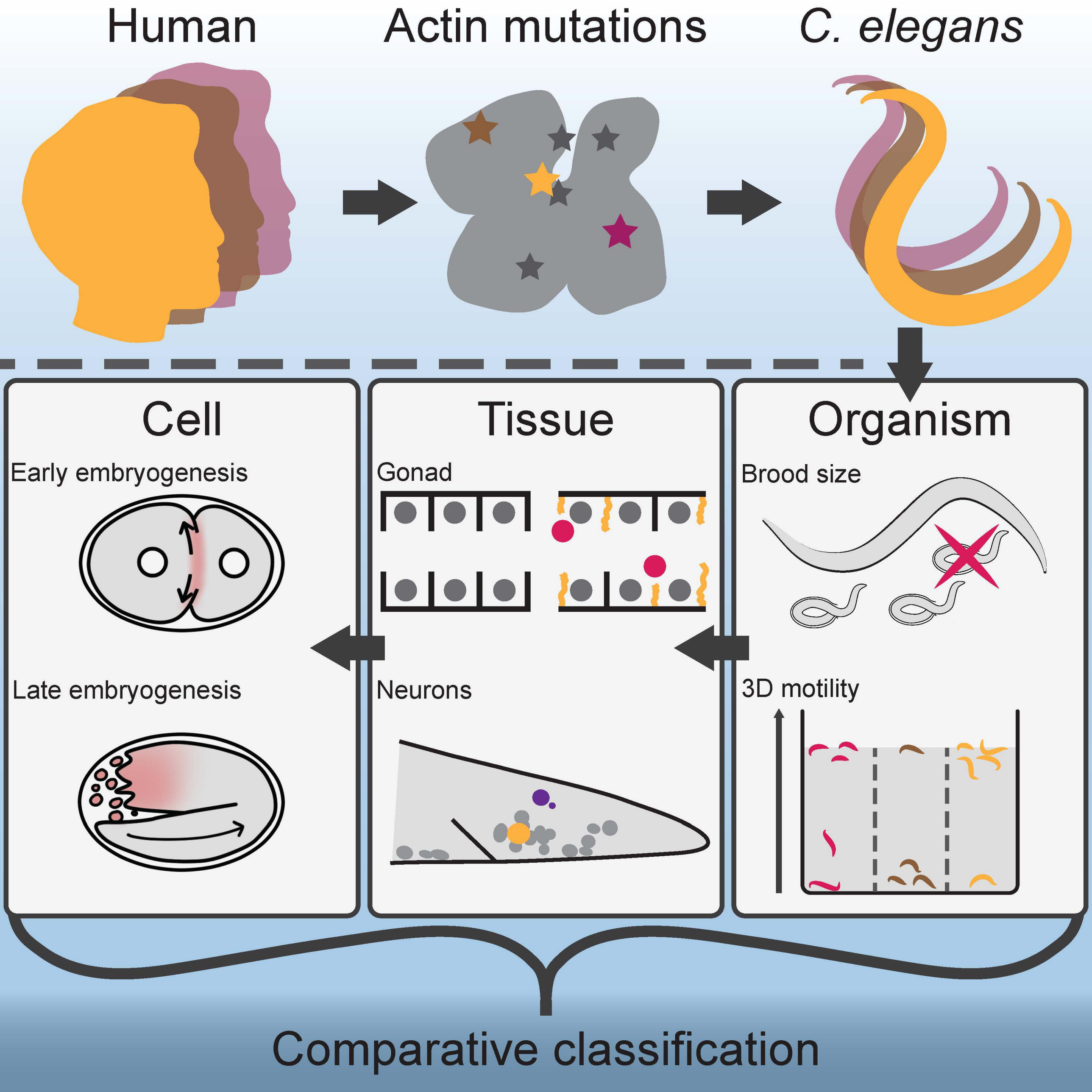
Human
Actin mutations
C. elegans
Cell
Early embryogenesis
Late embryogenesis
Tissue
Gonad
Neurons
Organism
Brood size
3D motility
Comparative classification

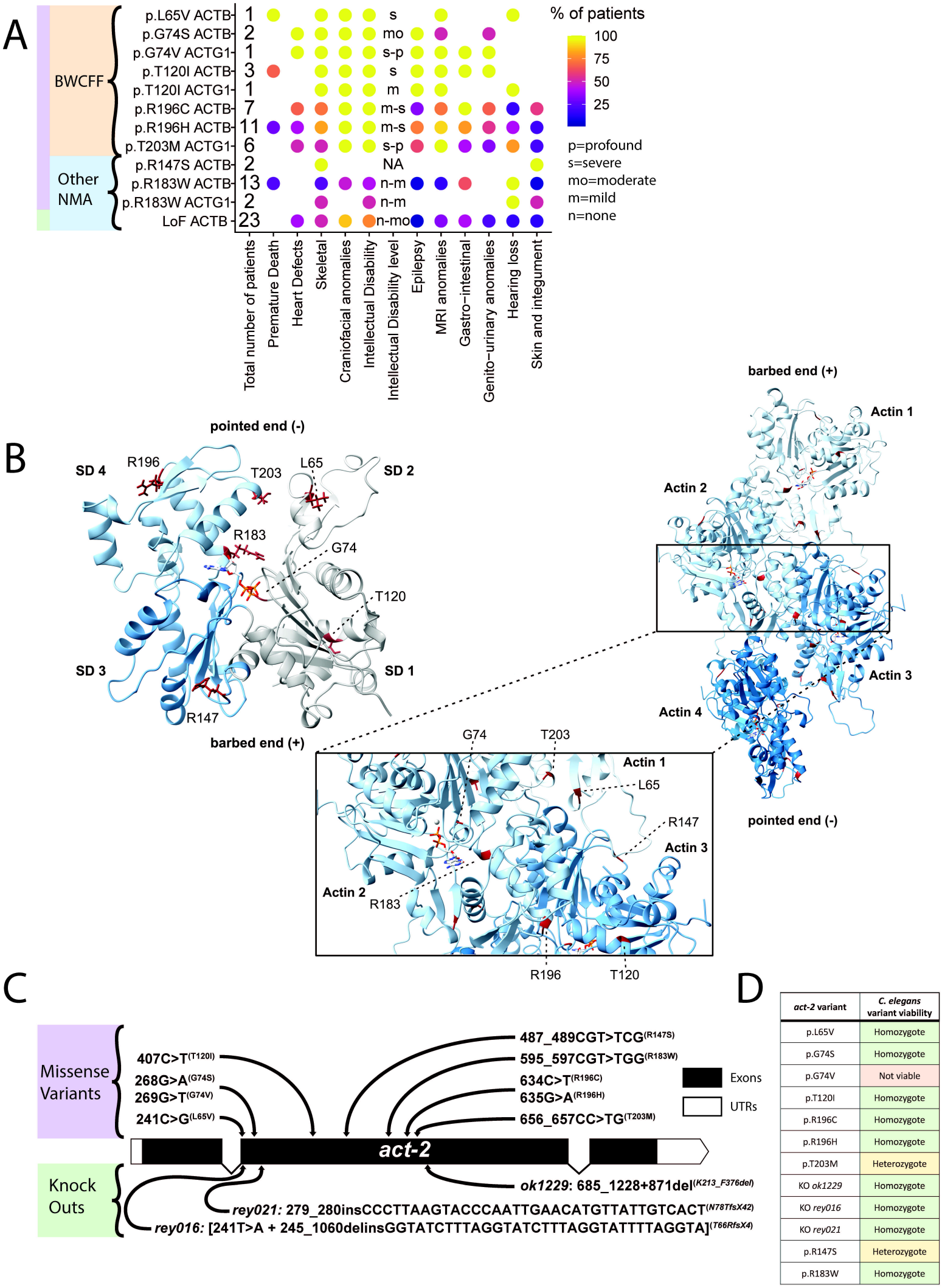

act-2 variant	C. elegans variant viability
p.L65V	Homozygote
p.G74S	Homozygote
p.G74V	Not viable
p.T120I	Homozygote
p.R196C	Homozygote
p.R196H	Homozygote
p.T203M	Heterozygote
KO *ok1229*	Homozygote
KO *rey016*	Homozygote
KO *rey021*	Homozygote
p.R147S	Heterozygote
p.R183W	Homozygote

Figure 1

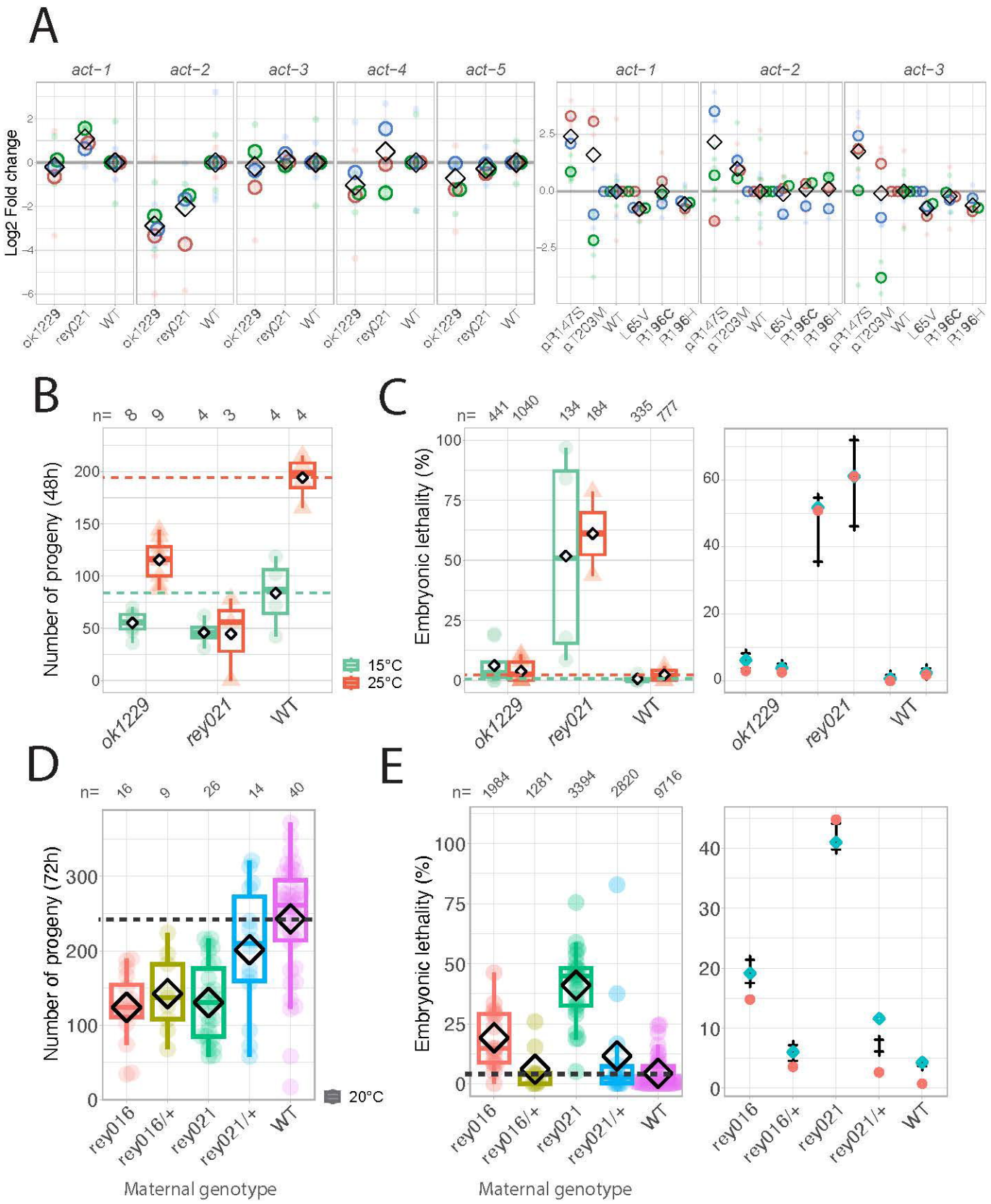
A
act-1
act-2
act-3
act-4
act-5
Log2 Fold change
ok1229
rey021
WT
pR147S
pT203M
L65V
R196C
R196H
B
n= 8 9 4 3 4 4
Number of progeny (48h)
15°C
25°C
C
n= 441 1040 134 184 335 777
Embryonic lethality (%)
D
n= 16 9 26 14 40
Number of progeny (72h)
20°C
rey016
rey016/+
rey021/+
Maternal genotype
E
n= 1984 1281 3394 2820 9716

Figure 2

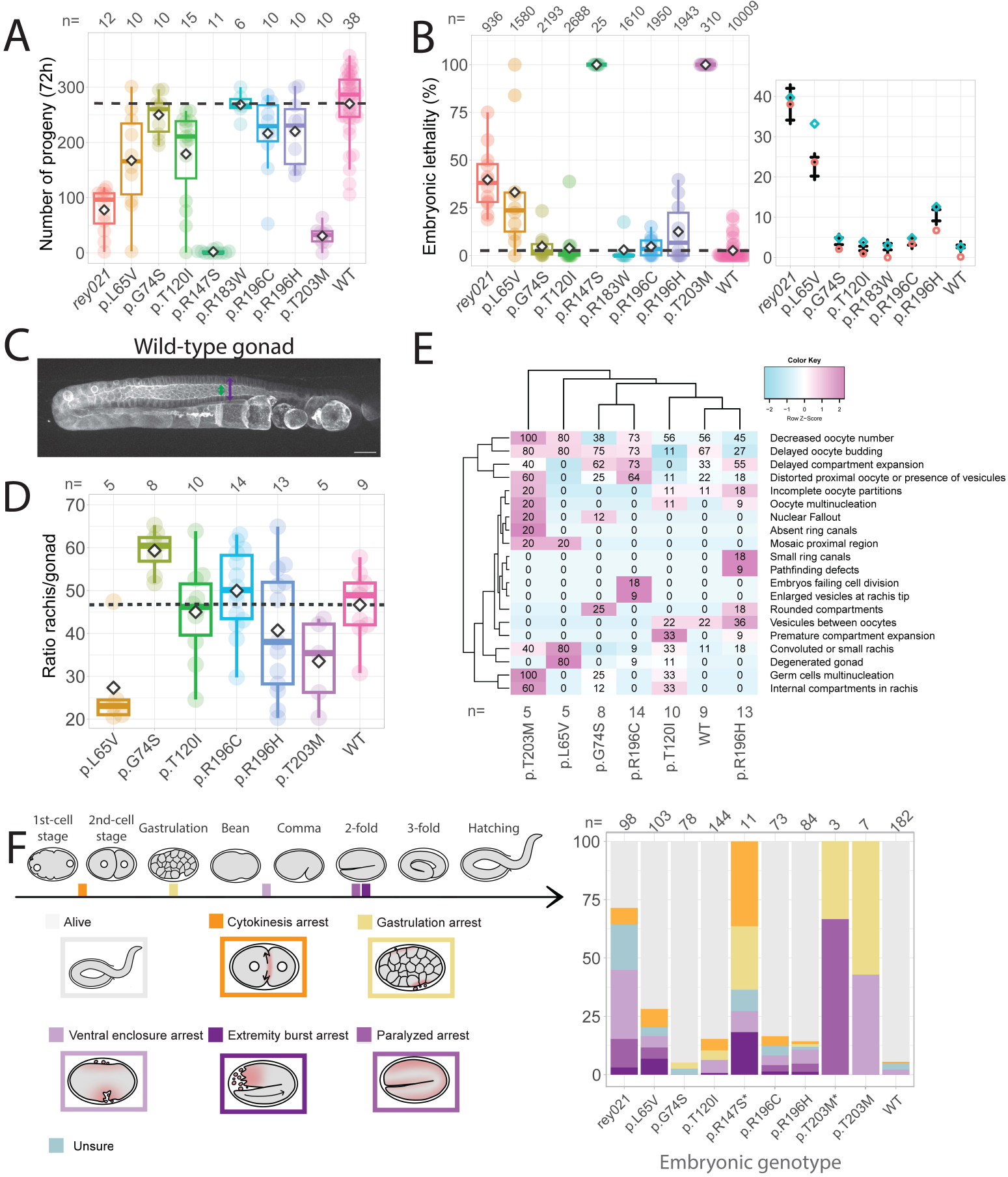
A
n= 12 10 10 15 11 6 10 10 10 38
Number of progeny (72h)
0 100 200 300
rey021 p.L65V p.G74S p.T120I p.R147S p.R183W p.R196C p.R196H p.T203M WT
B
n= 936 1580 2193 2688 25 1610 1950 1943 310 10009
Embryonic lethality (%)
0 25 50 75 100
0 10 20 30 40
rey021 p.L65V p.G74S p.T120I p.R147S p.R183W p.R196C p.R196H p.T203M WT
C
Wild-type gonad
D
n= 5 8 10 14 13 5 9
Ratio rachis/gonad
20 30 40 50 60 70
p.L65V p.G74S p.T120I p.R196C p.R196H p.T203M WT
E
Color Key
Row Z-Score
Decreased oocyte number
Delayed oocyte budding
Delayed compartment expansion
Distorted proximal oocyte or presence of vesicules
Incomplete oocyte partitions
Oocyte multinucleation
Nuclear Fallout
Absent ring canals
Mosaic proximal region
Small ring canals
Pathfinding defects
Embryos failing cell division
Enlarged vesicles at rachis tip
Rounded compartments
Vesicules between oocytes
Premature compartment expansion
Convoluted or small rachis
Degenerated gonad
Germ cells multinucleation
Internal compartments in rachis
n= 5 5 8 14 10 9 13
p.T203M p.L65V p.G74S p.R196C p.T120I WT p.R196H
F
1st-cell stage
2nd-cell stage
Gastrulation
Bean
Comma
2-fold
3-fold
Hatching
Alive
Cytokinesis arrest
Gastrulation arrest
Ventral enclosure arrest
Extremity burst arrest
Paralyzed arrest
Unsure
n= 98 103 78 144 11 73 84 3 7 182
0 25 50 75 100
rey021 p.L65V p.G74S p.T120I p.R147S* p.R196C p.R196H p.T203M* p.T203M WT
Embryonic genotype

Figure 3

A

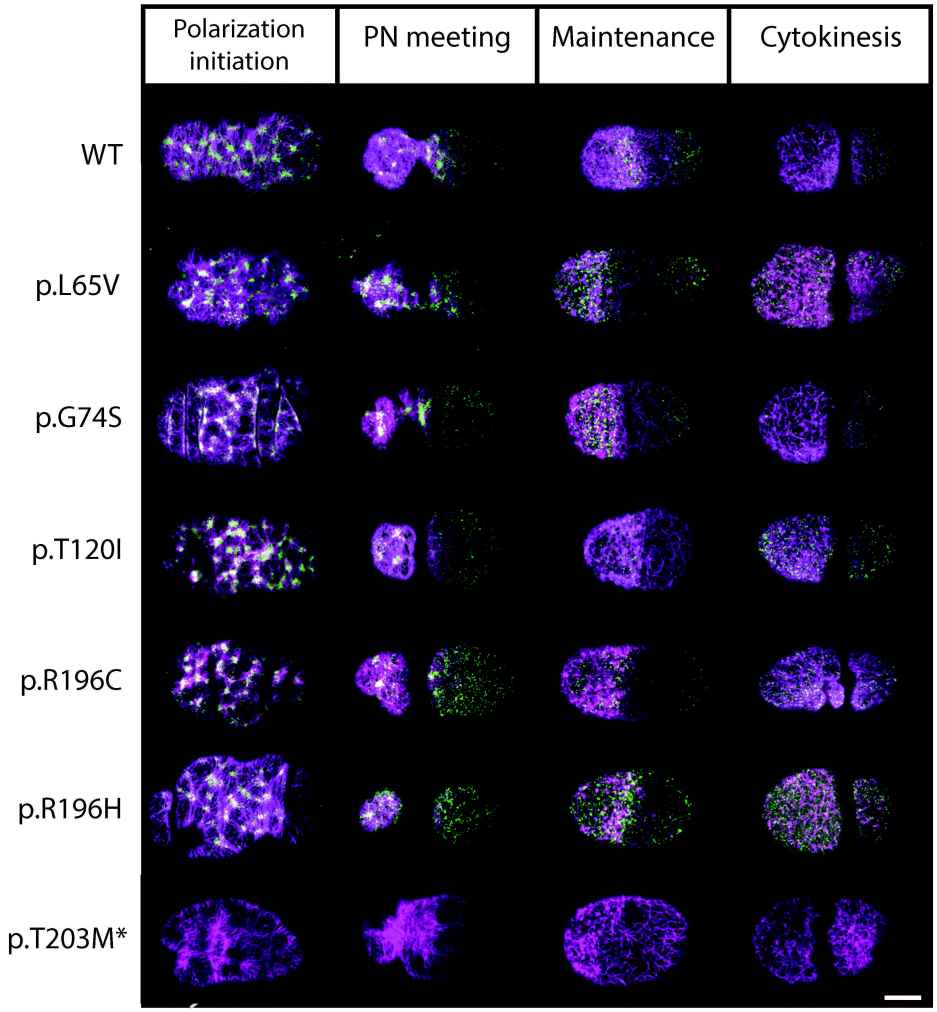

B

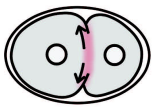

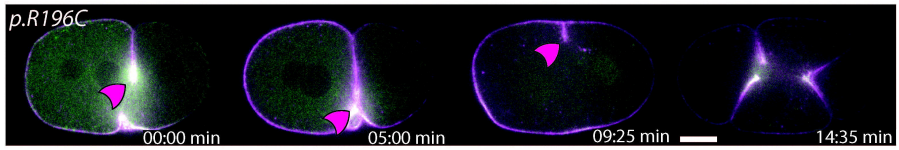

L65V	G74S	T120I	R196C	R196H	T203M*	WT
1/7	1/5	0/4	2/12	0/9	3/6	0/10

C

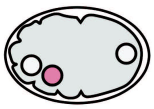

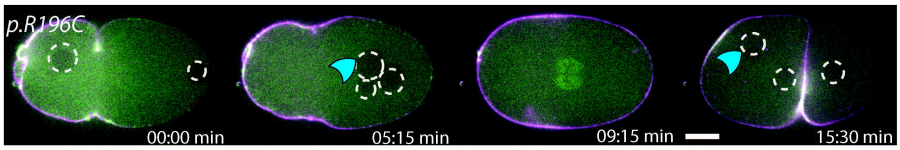

L65V	G74S	T120I	R196C	R196H	T203M*	WT
6/7	1/5	1/4	7/12	1/9	0/6	1/10

D

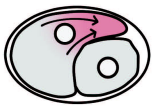

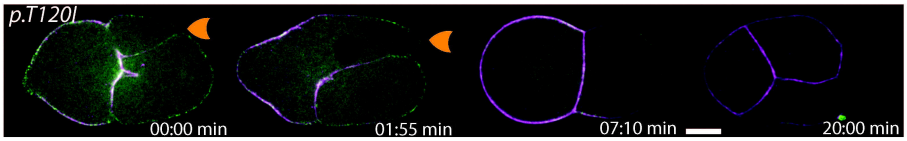

L65V	G74S	T120I	R196C	R196H	T203M*	WT
3/7	0/5	2/4	1/12	1/9	0/6	0/10

E

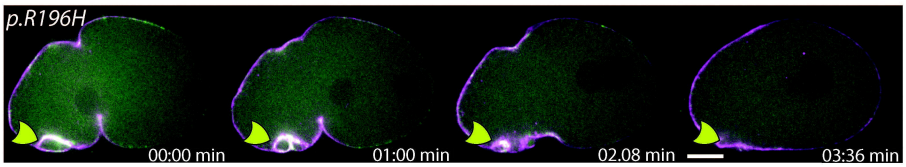

L65V	G74S	T120I	R196C	R196H	T203M*	WT
0/7	0/5	3/4	0/12	1/9	2/6	0/10

F

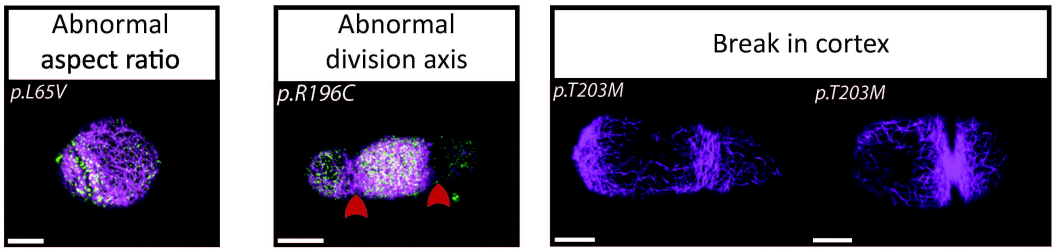

Figure 4

A

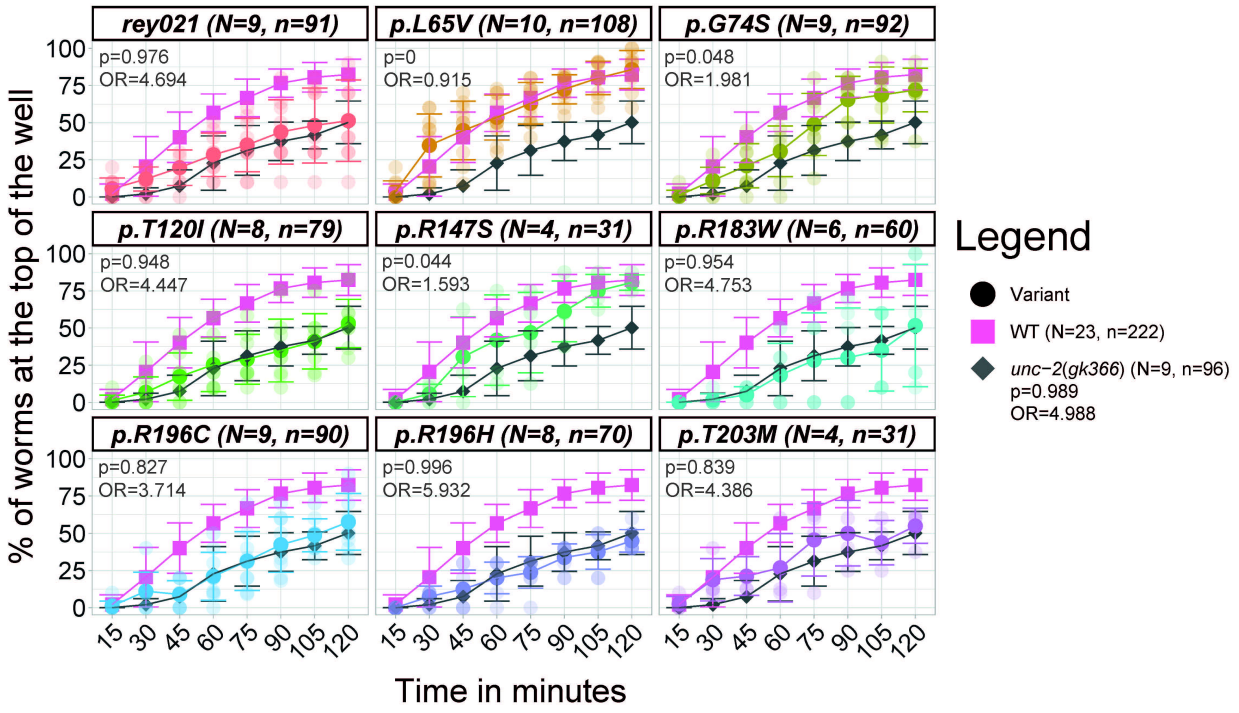

B

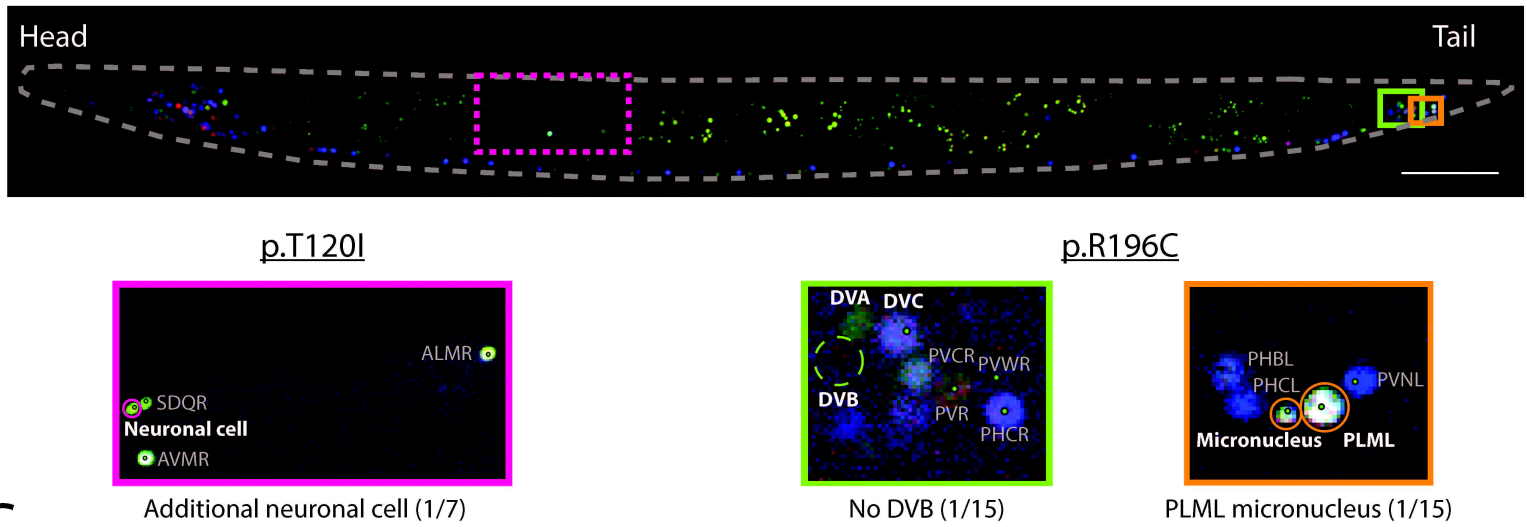

Additional neuronal cell (1/7)

No DVB (1/15)

PLML micronucleus (1/15)

C

		L65V	G74S	T120I	R147S	R196C	R196H	T203M	rey021	WT
Additional Neuron	SDQR	0/8	0/7	1/7	0/8	1/6	0/3	0/9	1/6	0/5
	Other	1/14	1/14	0/16	0/14	0/15	0/15	1/12	1/15	0/14
Micronucleus		0/14	0/14	0/16	1/14	1/15	0/15	1/12	2/15	0/14
Missing Neuron	DVB	0/14	1/14	0/16	0/14	1/15	0/15	0/12	1/15	0/14
	PDA	0/14	1/14	0/16	0/14	0/15	0/15	0/12	0/15	0/14
	Other	0/14	1/14	3/16	1/14	0/15	0/15	2/12	2/15	0/14

Figure 5

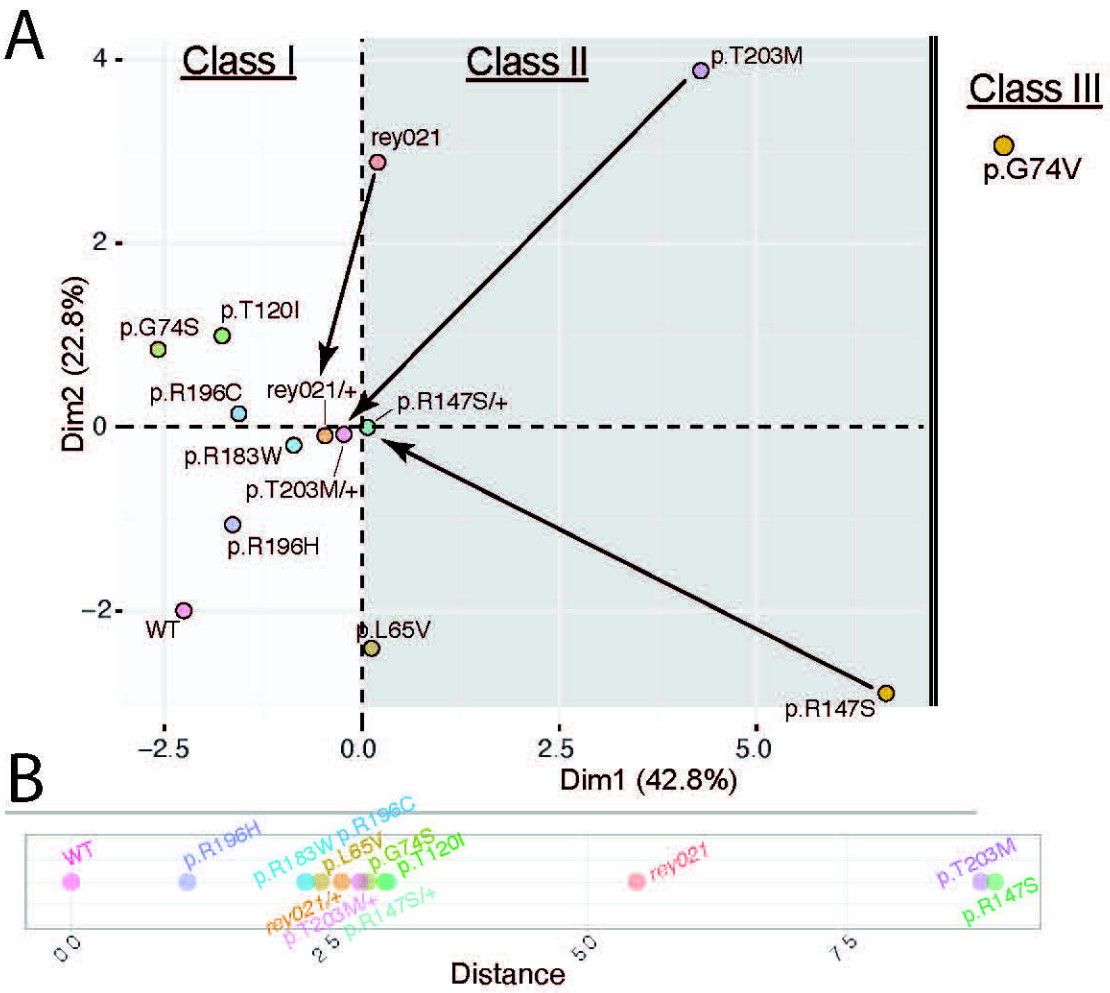
A
Class I
Class II
Class III
p.T203M
rey021
p.G74V
p.G74S
p.T120I
p.R196C
rey021/+
p.R147S/+
p.R183W
p.T203M/+
p.R196H
WT
p.L65V
p.R147S
Dim2 (22.8%)
Dim1 (42.8%)
4
2
0
−2
−2.5
0.0
2.5
5.0
B
WT
p.R196H
p.R183W
p.R196C
p.L65V
p.G74S
p.T120I
rey021
p.T203M
p.R147S
rey021/+
p.T203M/+
p.R147S/+
0.0
2.5
5.0
7.5
Distance

Figure 6

A

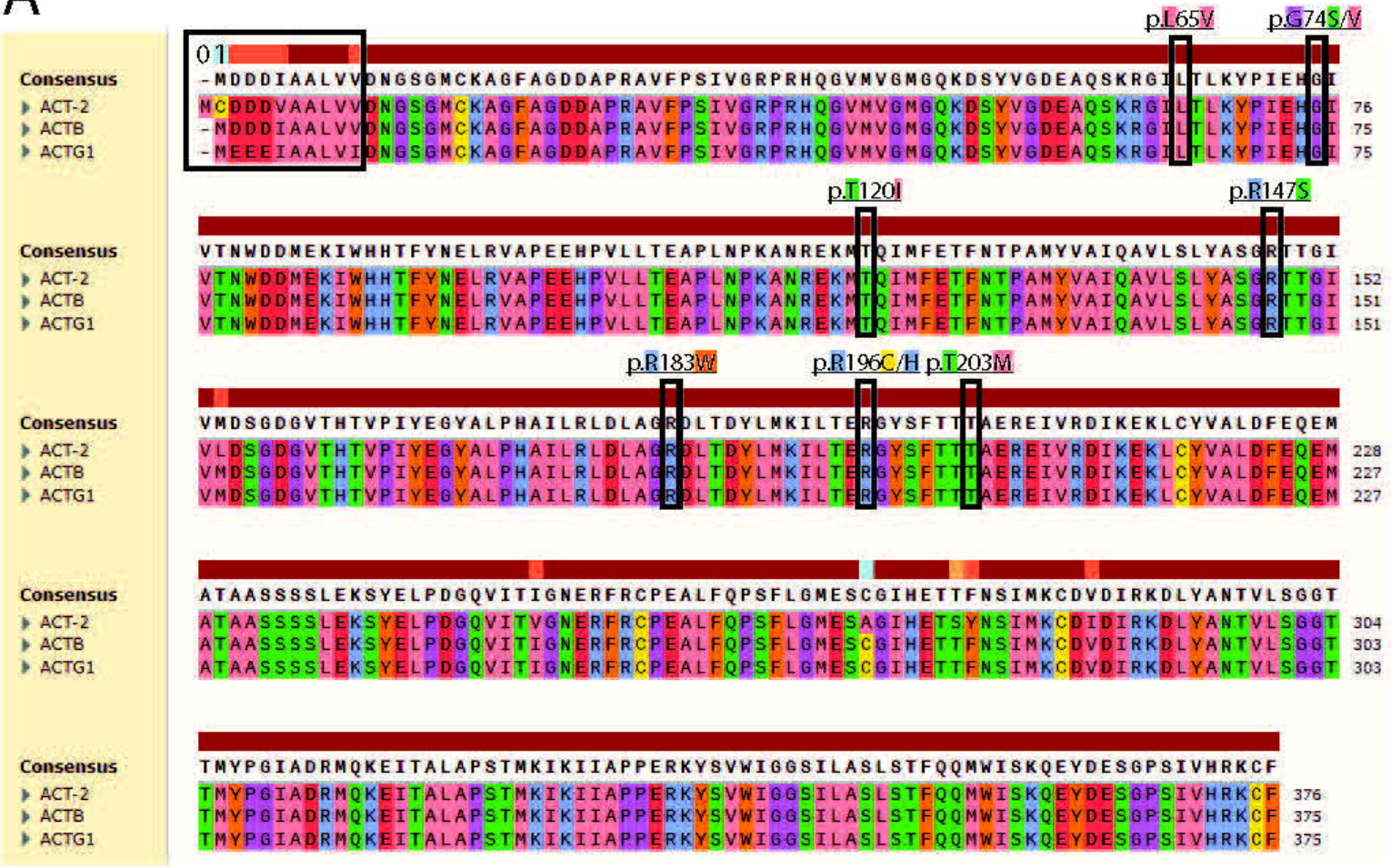
p.L65V
p.G74S/V
p.T120I
p.R147S
p.R183W
p.R196C/H
p.T203M
Consensus
ACT-2
ACTB
ACTG1

B

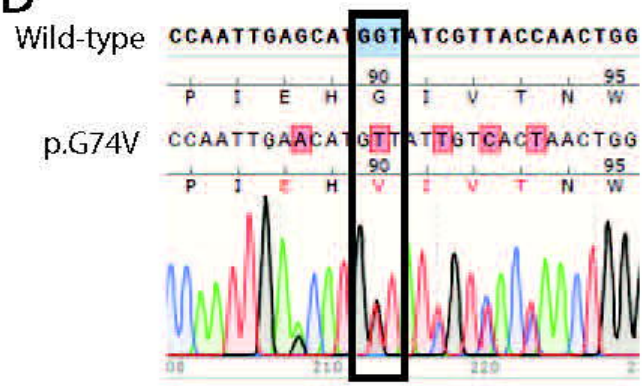
Wild-type
CCAATTGAGCATGGTATCGTTACCAACTGG
p.G74V
CCAATTGAACATGTTATTGTCACTAACTGG

Figure S1

$$E = 10^{\frac{1}{slope}}$$

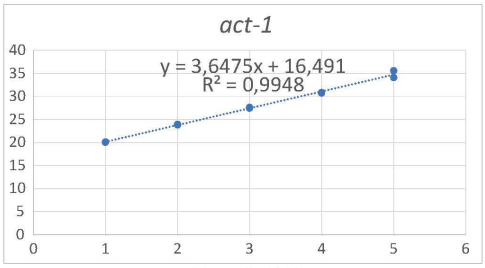

E = 1.88

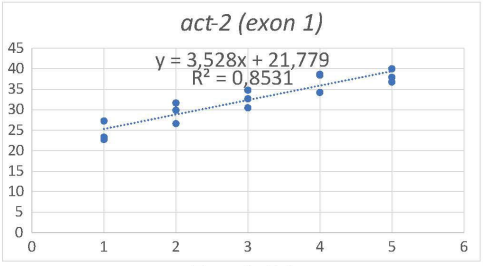

E = 1.92

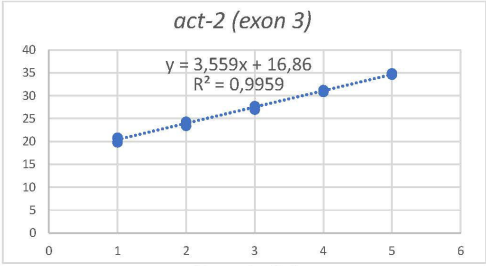

E = 1.91

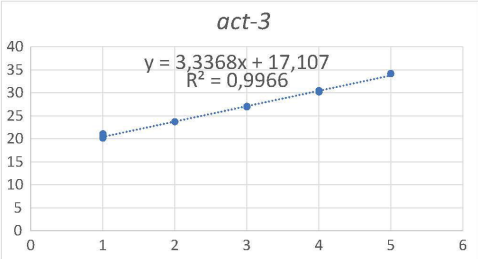

E = 1.99

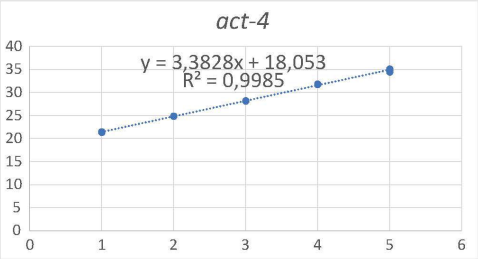

E = 1.97

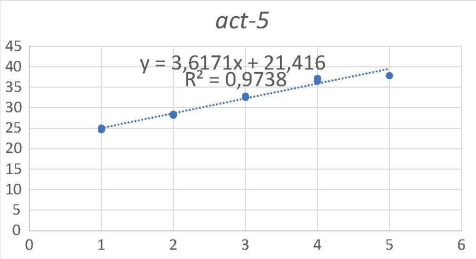

E = 1.89

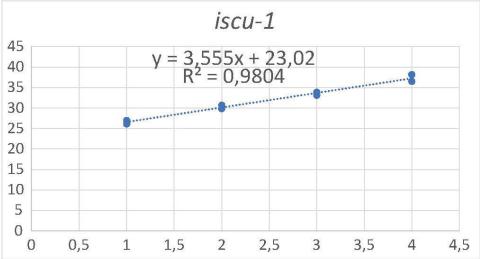

E = 1.91

Figure S2

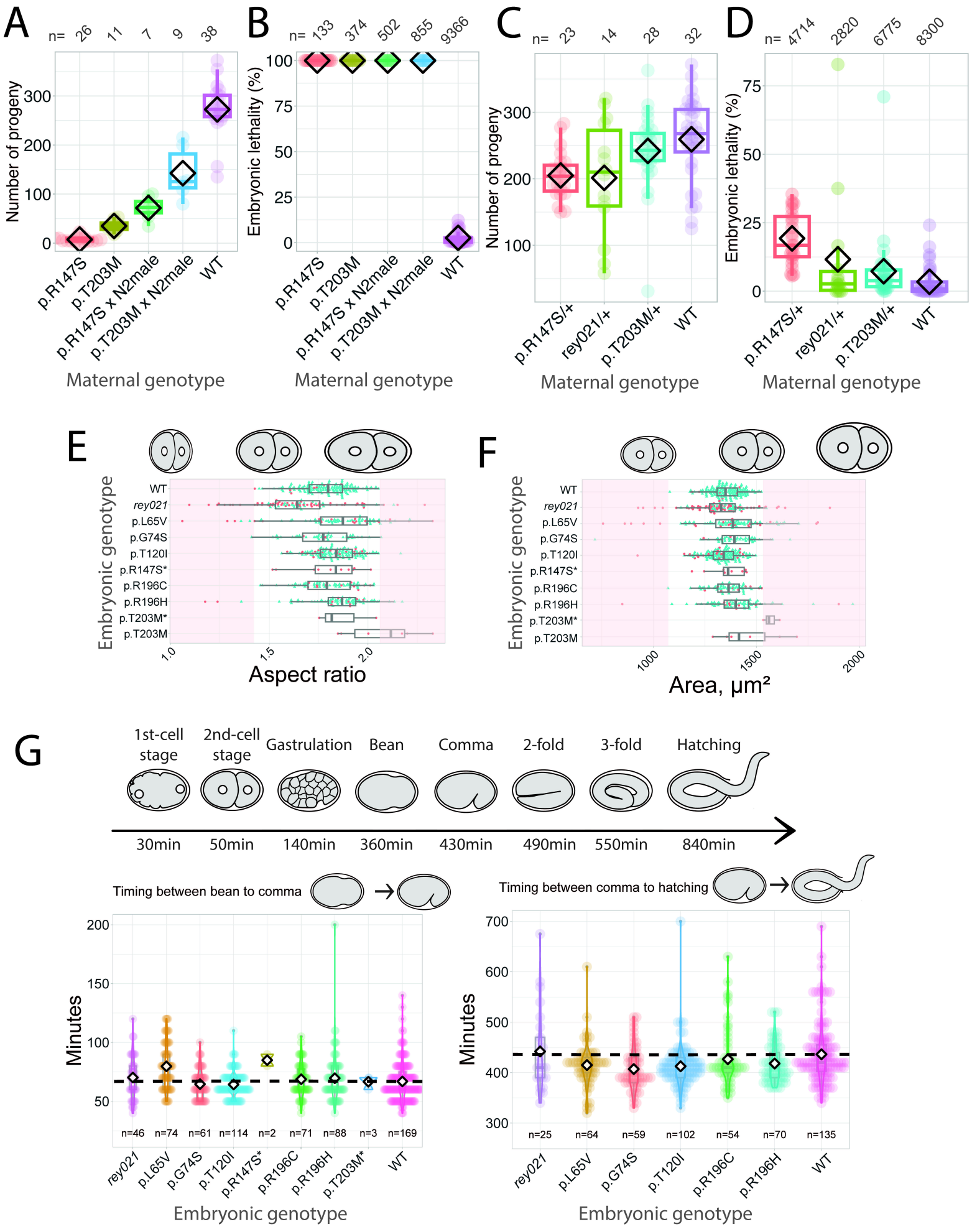
A
n= 26 11 7 9 38
Number of progeny
0
100
200
300
p.R147S
p.T203M
p.R147S x N2male
p.T203M x N2male
WT
Maternal genotype
B
n= 133 374 502 855 9366
Embryonic lethality (%)
0
25
50
75
100
p.R147S
p.T203M
p.R147S x N2male
p.T203M x N2male
WT
Maternal genotype
C
n= 23 14 28 32
Number of progeny
100
200
300
p.R147S/+
rey021/+
p.T203M/+
WT
Maternal genotype
D
n= 4714 2820 6775 8300
Embryonic lethality (%)
0
25
50
75
p.R147S/+
rey021/+
p.T203M/+
WT
Maternal genotype
E
Embryonic genotype
WT
rey021
p.L65V
p.G74S
p.T120I
p.R147S*
p.R196C
p.R196H
p.T203M*
p.T203M
1.0
1.5
2.0
Aspect ratio
F
Embryonic genotype
WT
rey021
p.L65V
p.G74S
p.T120I
p.R147S*
p.R196C
p.R196H
p.T203M*
p.T203M
1000
1500
2000
Area, µm²
G
1st-cell stage
2nd-cell stage
Gastrulation
Bean
Comma
2-fold
3-fold
Hatching
30min
50min
140min
360min
430min
490min
550min
840min
Timing between bean to comma
Minutes
50
100
150
200
n=46 n=74 n=61 n=114 n=2 n=71 n=88 n=3 n=169
rey021
p.L65V
p.G74S
p.T120I
p.R147S*
p.R196C
p.R196H
p.T203M*
WT
Embryonic genotype
Timing between comma to hatching
Minutes
300
400
500
600
700
n=25 n=64 n=59 n=102 n=54 n=70 n=135
rey021
p.L65V
p.G74S
p.T120I
p.R196C
p.R196H
WT
Embryonic genotype

Figure S3

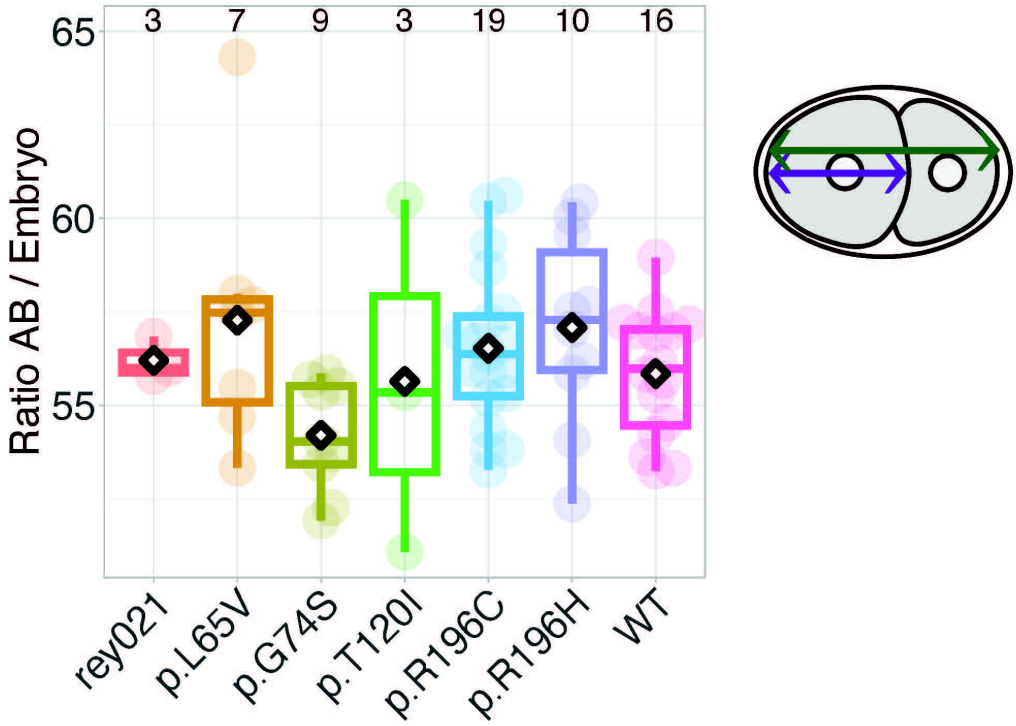
3
7
9
3
19
10
16
65
60
55
Ratio AB / Embryo
rey021
p.L65V
p.G74S
p.T120I
p.R196C
p.R196H
WT

Figure S4

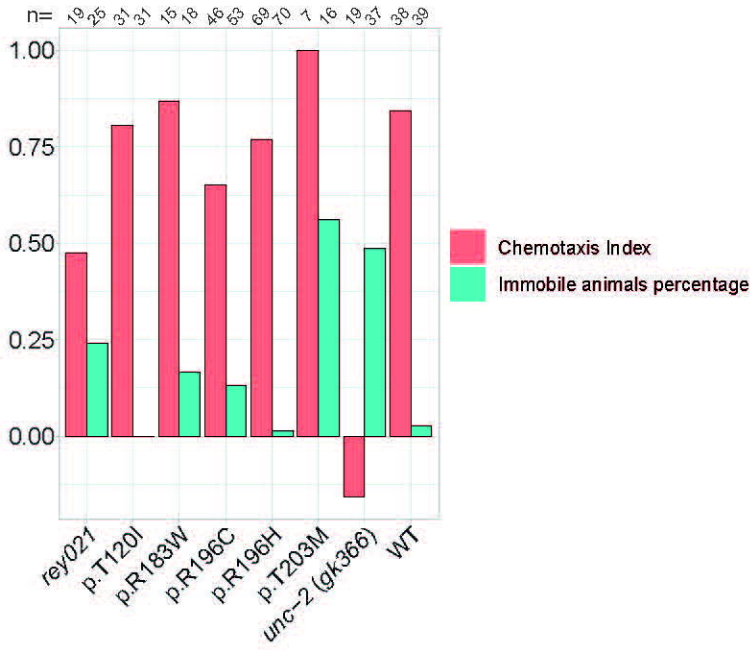
n=
19
25
31
31
15
18
46
53
69
70
7
16
19
37
38
39
1.00
0.75
0.50
0.25
0.00
rey021
p.T120I
p.R183W
p.R196C
p.R196H
p.T203M
unc-2 (gk366)
WT
Chemotaxis Index
Immobile animals percentage

Figure S5

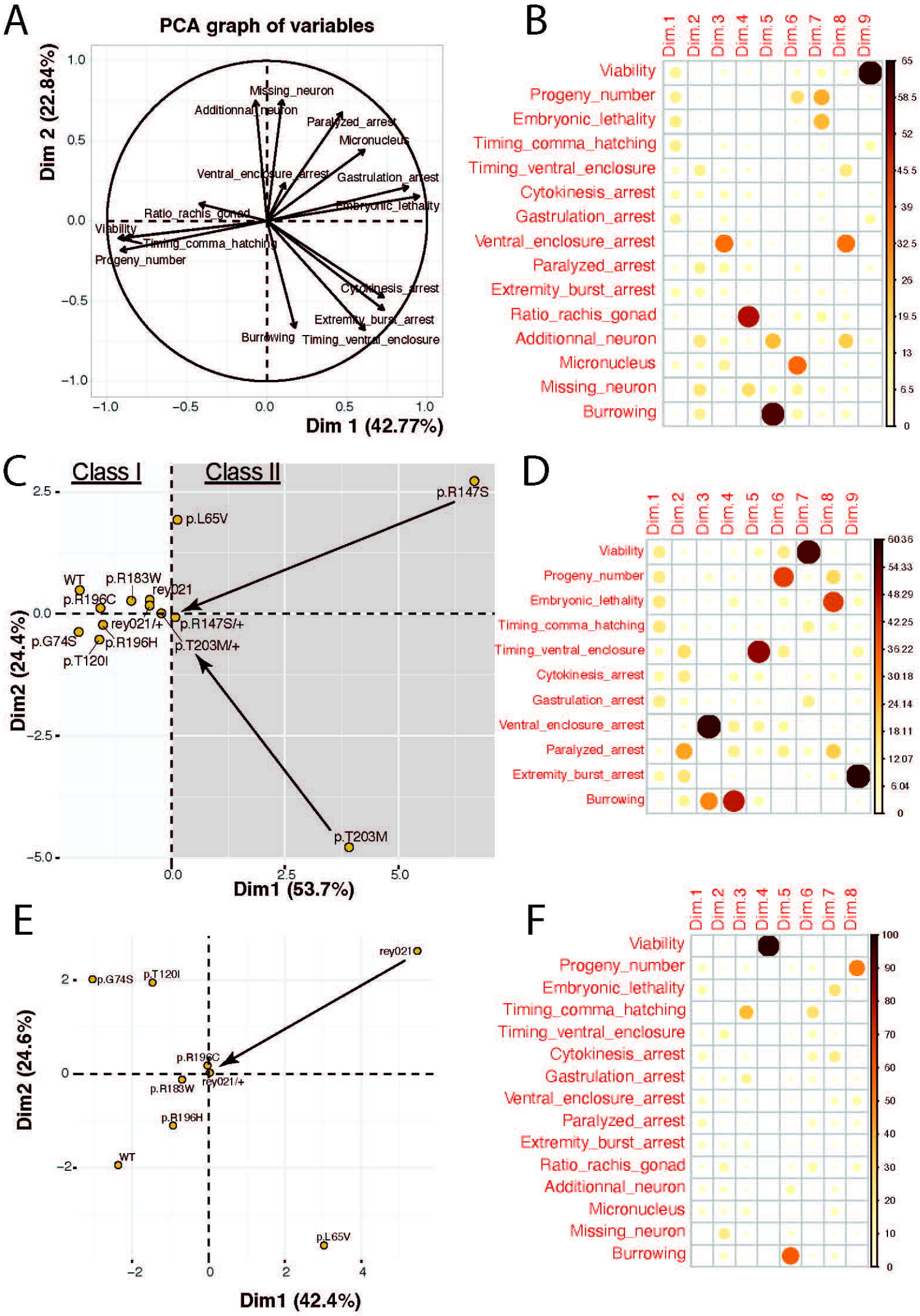
A
PCA graph of variables
Dim 2 (22.84%)
Dim 1 (42.77%)
Missing_neuron
Additionnal_neuron
Paralyzed_arrest
Micronucleus
Ventral_enclosure_arrest
Gastrulation_arrest
Embryonic_lethality
Ratio_rachis_gonad
Viability
Timing_comma_hatching
Progeny_number
Cytokinesis_arrest
Extremity_burst_arrest
Burrowing
Timing_ventral_enclosure
B
Dim.1
Dim.2
Dim.3
Dim.4
Dim.5
Dim.6
Dim.7
Dim.8
Dim.9
Viability
Progeny_number
Embryonic_lethality
Timing_comma_hatching
Timing_ventral_enclosure
Cytokinesis_arrest
Gastrulation_arrest
Ventral_enclosure_arrest
Paralyzed_arrest
Extremity_burst_arrest
Ratio_rachis_gonad
Additionnal_neuron
Micronucleus
Missing_neuron
Burrowing
C
Class I
Class II
p.R147S
p.L65V
WT
p.R183W
rey021
p.R196C
rey021/+
p.R147S/+
p.G74S
p.R196H
p.T203M/+
p.T120I
p.T203M
Dim2 (24.4%)
Dim1 (53.7%)
D
Viability
Progeny_number
Embryonic_lethality
Timing_comma_hatching
Timing_ventral_enclosure
Cytokinesis_arrest
Gastrulation_arrest
Ventral_enclosure_arrest
Paralyzed_arrest
Extremity_burst_arrest
Burrowing
E
rey021
p.G74S
p.T120I
p.R196C
p.R183W
rey021/+
p.R196H
WT
p.L65V
Dim2 (24.6%)
Dim1 (42.4%)
F
Viability
Progeny_number
Embryonic_lethality
Timing_comma_hatching
Timing_ventral_enclosure
Cytokinesis_arrest
Gastrulation_arrest
Ventral_enclosure_arrest
Paralyzed_arrest
Extremity_burst_arrest
Ratio_rachis_gonad
Additionnal_neuron
Micronucleus
Missing_neuron
Burrowing

Figure S6